Naval Research Laboratory
Washington, DC 20375-5320

NRL/MR/6720--96-7812

A Detailed Characterization of Power Flow and PRS Performance on Phoenix

R.E. Terry
K.G. Whitney
J. Davis
J.L. Giuliani, Jr.
J. Rogerson

Radiation Hydrodynamics Branch
Plasma Physics Division

F.L. Cochran

Berkeley Research Associates
Springfield, VA

J. Draper
J. Miller
E. Nolting

Naval Surface Warfare Center
White Oak, MD

May 3, 1996

Approved for public release; distribution unlimited.

REPORT DOCUMENTATION PAGE

Form Approved
OMB No. 0704-0188

1. AGENCY USE ONLY *(Leave Blank)*

2. REPORT DATE

May 3, 1996

3. REPORT TYPE AND DATES COVERED

4. TITLE AND SUBTITLE

A Detailed Characterization of Power Flow and PRS Performance on Phoenix

5. FUNDING NUMBERS

6. AUTHOR(S)

R.E. Terry, K.G. Whitney, J. Davis, J.L. Giuliani, Jr., J. Rogerson, F.L. Cochran J. Draper, J. Miller, and E. Nolting

7. PERFORMING ORGANIZATION NAME(S) AND ADDRESS(ES)

Naval Research Laboratory
Washington, DC 20375-5320

8. PERFORMING ORGANIZATION REPORT NUMBER

NRL/MR/6720--96-7812

9. SPONSORING/MONITORING AGENCY NAME(S) AND ADDRESS(ES)

Defense Nuclear Agency
TDSP
Alexandria, VA 22310

10. SPONSORING/MONITORING AGENCY REPORT NUMBER

11. SUPPLEMENTARY NOTES

This research was sponsored by the Defense Nuclear Agency under Job Order Title, "Phoenix Support," MIPR Nos. 95-2100, 94-1668, and 96-2070

12a. DISTRIBUTION/AVAILABILITY STATEMENT

Approved for public release; distribution unlimited.

12b. DISTRIBUTION CODE

13. ABSTRACT *(Maximum 200 words)*

This study first constructs a complete model of the Phoenix pulser and its puff gas load, connects the model with experimental findings, and then suggests some means of improving the pulser's K shell x-ray yield. A numerical study of energy coupling into a dummy resistive load showed that an output impedance of about 1 Ω would minimize the reflected energy; from this result a thevenin equivalent circuit was constructed. Use of the transmission line model to study the Phoenix pre-pulse evolved to a study of early power flow and has produced a breakdown model that contains a detailed field map for the PRS load cavity, a mapping of the computed electric field values onto the grid of neutral gas density measurements, and a simple ionization model. Preliminary results from the breakdown model indicate ionization regions consistent with the observed "reversed" zippering, and a Boltzmann solution in those regions shows that at 40% of peak field the ionization would proceed in about 6 ns. A series of full 1D MHD studies, equipped with both CRE and time dependent ionization and excited state models, has refined the expected yields for Ar gas to about 18 kJ using a 4 cm long, shell of 0.375 mgm mass.

14. SUBJECT TERMS

Z-pinch physics
Plasma radiation sources
Radiation MHD

15. NUMBER OF PAGES

59

16. PRICE CODE

17. SECURITY CLASSIFICATION OF REPORT	18. SECURITY CLASSIFICATION OF THIS PAGE	19. SECURITY CLASSIFICATION OF ABSTRACT	20. LIMITATION OF ABSTRACT
UNCLASSIFIED	UNCLASSIFIED	UNCLASSIFIED	UL

CONTENTS

EXECUTIVE SUMMARY

The primary requirement in any DNA program for Phoenix is an understanding of the machine's performance, the definitive characterization of that performance, and a documentation of strategies for the optimization of that performance. The present study addresses these goals by first constructing a complete model of the pulser and its puff gas load, connecting the model with experimental findings, and then suggesting some means of improving the pulser's K shell x-ray yield.

The full transmission line model of the Phoenix pulser includes all elements in the device, except for a divertor switch in oil near the Marx bank which is not relevant until after the PRS has imploded. From the full model a numerical study of energy coupling into a dummy resistive load showed that a proper output impedance of about 1 Ω would minimize the reflected energy. Using the voltage waveform presented at the insulator stack at that match point, a Thevenin equivalent circuit was constructed for use in driving 1D and 2D radiation hydrodynamic models. The equivalent circuit can also be used to drive an abbreviated "Screamer" transmission line model, as well as the transmission line model used in earlier work[1]. Four slightly different numerical models of Phoenix are now available for comparison with experiment.

Care has been taken to arrange model test points at proper locations in order to benchmark the numerical images of Phoenix with the experimental images derived from several physical voltage and current monitors along the pulse line. Recent short circuit shot events have not been very numerous, but a comparison of the "full" numerical model to a representative shot is quite encouraging, and reveals one inconsistent voltage monitor (on the first transformer) in need of recalibration. Further examination of the voltage waveform on the pulse forming line revealed a need to improve the numerical model of the output switch from the transfer capacitor (TC).

The improved TC switch model has resulted in good agreement with experiment and has allowed a rather detailed study of prepulse voltage at the load, where there is no experimental diagnostic. It is possible that the expected prepulse is sufficient to start breakdown in the gas puff load and that the pattern of that breakdown may figure significantly in determining the amount of gas imploded. A detailed numerical study of $\frac{E}{p}$ has been constructed to check out the implications of the prepulse waveform inferred from the numerical model.

The model of early power flow in Phoenix has evolved to contain four elements, and any other gas puff PRS device could also benefit from a similar analysis. First, a detailed field map for the PRS load cavity was constructed with full attention to the details of the geometry. The field model has been thoroughly explored for the neutral gas limit but it can (and must) treat the case of finite electrical conductivity as well. Second, a mapping of the computed electric field values onto the grid of neutral gas density measurements (due to Peterson and Weber) was constructed to provide a starting value of E/N. Third, a simple ionization model from largely experimental Ar data was constructed to identify the likely breakdown domains. This model was later augmented by a Boltzmann solver equipped with a more detailed atomic Ar model. Fourth, an input protocol to feed the initial conductivity into the PRISM 2D MHD code was explored to examine the implications for load zippering as view by the existing Phoenix diagnostic array.

Preliminary results of the breakdown model indicate ionization regions consistent with the observed “reversed” zippering, and the Boltzmann solution in those regions indicated that at 40 % of peak field the ionization would proceed in about 6 ns. A campaign of pinhole camera images was also planned to compare with the results of this study, but due to general facility delays, it must now await further efforts.

The present version of the full transmission line model permits the calculation of load kinetic energy imparted to a reactionless slug by the output pulse. A survey of $m_o R_o^2$ values relevant to gas and Al wire loads has identified domains of optimal kinetic energy transfer under those electrical conditions which should be achieved once the new insulator stack is fielded.

In addition, using the equivalent circuit identified above and a subset of transmission line elements for the front end, a series of full 1D MHD studies, equipped with both CRE and time dependent ionization and excited state models, has further refined the expected yields for the pulser. For Ar gas the best expected yields are about 18 kJ using a 4 cm long, well defined shell with a mass of 0.375 mgm.

A DETAILED CHARACTERIZATION OF POWER FLOW AND PRS PERFORMANCE ON PHOENIX

I. BASELINE POWER FLOW CHARACTERIZATION

Phoenix comprises (i) a Marx bank and oil output line, (ii) a water line transfer capacitor and switch, (iii) a pulse forming line, switched onto the first transformer (in water), (iv) a prepulse suppression switch, (v) a second water transformer (terminated in a radial taper and vacuum insulator stack), (vi) a constant impedance biconic output line, (vii) a variable impedance conical MITL, and (viii) a load chamber.

A. Line Model Elements

The Phoenix model discussed here is a definitive one in that all relevant elements are described and all the power flow details upstream of the voltage monitors in the second water transformer are modeled. In the table below, each element is assigned a lumped inductance or capacitance, while

Table I.1 Phoenix Full Line Elements

Line Component	Delay Time [ns]	Impedance [Ω]	L or C [nH] or [nF]	**Monitor Name** Comments
Marx Capacitance	-	-	97	·
Marx Series Res.	-	1.0E6 → 2	-	variable, τ_d 1 ns
Marx Series Ind.	-	-	5300	**Marx** Voltage, Current
Oil Line	25.0	41.0	-	"dogleg"
Trans Cap Shunt Res.	-	720	-	·
Trans Cap Tline	47.0	5.0	235.0	·
Trans Cap Tline	8.0	4.6	36.8	·
Trans Cap Tline	8.0	3.1	24.8	·
Trans Cap Tline	80.0	2.1	168.0	**TCap** Voltage
Trans Cap Tline	10.0	2.3	23.0	·
Trans Cap Tline	13.0	2.6	33.8	·
Trans Cap Shunt Res.	-	720	-	·
Trans Cap Series Res.	1225	1.0E3→ 0	-	variable, τ_d 15→50 ns
Trans Cap Switch Br.	1300	1.0E6→ 0	-	variable, τ_d 1 ns
PFL Shunt Res.	-	1,070	-	·
PFL Tline	11	2.65	29.15	·
PFL Tline	6	1.61	9.66	·
PFL Tline	35.0	1.3	45.5	**PFL** Voltage
PFL Tline	6	1.7	10.2	·
PFL Shunt Res.	-	1,070	-	·
PFL Switch Br.	1677	1.0E6 → 0.1	-	variable, τ_d 2 ns
1st Trans Tline	7	1.6	11.2	·
1st Trans Tline	21	1.2	25.2	**1st Transformer**
1st Trans Tline	7	1.5	10.5	Voltage

Manuscript approved January 31, 1996.

Table I.1 (cont) Phoenix Full Line Elements

Line Component	Delay Time [ns]	Impedance [Ω]	L or C [nH] or [nF]	**Monitor Name** Comments
1st Trans Tline	7	1.95	13.65	·
1st Trans Shunt Cap	-	-	0.2	·
Prepulse Switch Br.	1725	1.0E6 →0.01	-	variable, τ_d 2 ns
2nd Trans Tline	3.0	2.0	6.0	·
2nd Trans Tline	3.0	1.5	4.5	·
2nd Trans Tline	7.0	1.3	9.1	·
2nd Trans Tline	50.0	1.15 to 0.83	-	linear Z profile
2nd Trans Tline	5.0	0.75	3.75	·
Rad. Water Taper	5.0	0.7	3.50	·
Rad. Water Taper	15.0	0.65	9.75	·
Rad. Water Taper	5.0	0.64	3.20	·
Rad. Water Taper	5.0	0.62	3.10	·
Rad. Water Taper	5.5	0.72	3.96	**Water Monitors**
Water Flare A	2.0	0.73	1.46	Voltage, Current
Water Flare B	1.0	1.32	1.32	·
Water Flare C	2.5	1.36	3.40	·
Water Flare D	1.0	1.90	1.90	E_{out}, optional
Plastic	0.1	12.15	1.215	flashover shunt
Vacuum Flare A	0.2	13.67	2.734	·
Vacuum Flare B	0.2	10.15	2.03	**Tube Current**
Vacuum Flare C	0.3	3.15	0.945	·
Const Z MITL	0.9	2.0	1.80	**Vac. Feed Current.**
Const Gap MITL no.1	0.1	2.08936	⇓	summed
Const Gap MITL no.2	0.1	2.36549	·	·
Const Gap MITL no.3	0.1	2.81632	·	·
Const Gap MITL no.4	0.1	3.48224	·	·
Const Gap MITL no.5	0.1	4.56967	·	·
Const Gap MITL no.6	0.1	6.68900	·	·
Const Gap MITL no.7	0.1	8.12275	21.094	inductance
Final Feed	0.1	13.4	1.34	·

“delay time” usually refers to the signal transit time across an element; “impedance,” to the local ratio of line voltage to line current; and τ_d, to the e-folding time of a variable element, usually a resistance. In the case of variable elements the “delay time” is the required offset from the time origin before variation in time begins. The existing test points are named and the waveform arising from them is listed. A transmission line diagram of the model is shown in Fig. I.1.

Short Line Model

The voltage waveform inferred from the water voltage monitor (called Tube Voltage or VT

Fig I.1

PHOENIX LINE MODEL
16 nh 0.5 mΩ Short

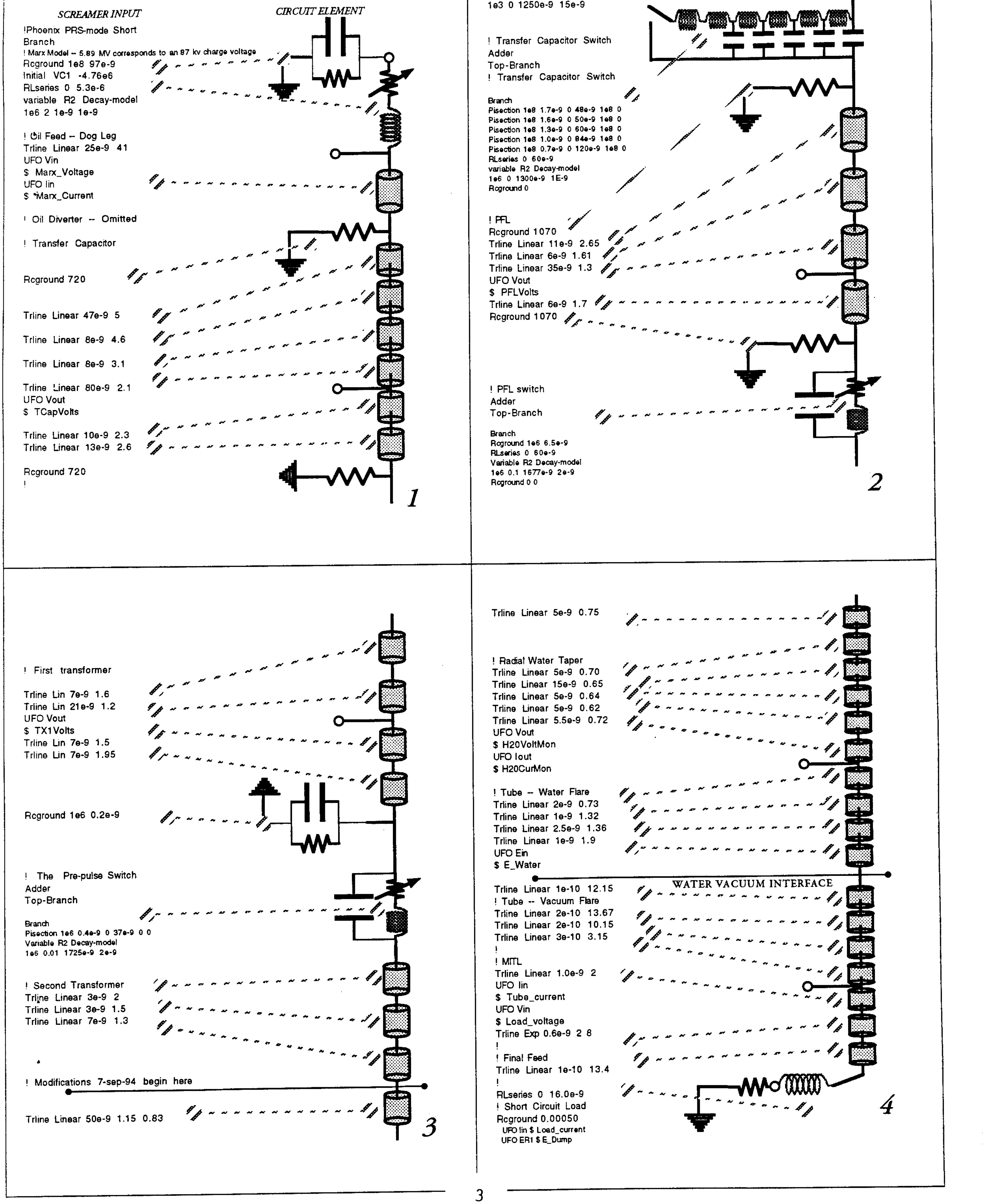

```
!Phoenix PRS-mode Short
Branch
! Marx Model -- 5.89 MV corresponds to an 87 kv charge voltage
Rcground 1e8 97e-9
Initial VC1 -4.76e6
RLseries 0 5.3e-6
variable R2 Decay-model
1e6 2 1e-9 1e-9

! Oil Feed -- Dog Leg
Trline Linear 25e-9 41
UFO Vin
$ Marx_Voltage
UFO Iin
$ Marx_Current

! Oil Diverter -- Omitted

! Transfer Capacitor

Rcground 720

Trline Linear 47e-9 5

Trline Linear 8e-9 4.6

Trline Linear 8e-9 3.1

Trline Linear 80e-9 2.1
UFO Vout
$ TCapVolts

Trline Linear 10e-9 2.3
Trline Linear 13e-9 2.6

Rcground 720
!
```

```
RLseries 0 0
variable R2 Decay-model
1e3 0 1250e-9 15e-9

! Transfer Capacitor Switch
Adder
Top-Branch
! Transfer Capacitor Switch

Branch
Pisection 1e8 1.7e-9 0 48e-9 1e8 0
Pisection 1e8 1.6e-9 0 50e-9 1e8 0
Pisection 1e8 1.3e-9 0 60e-9 1e8 0
Pisection 1e8 1.0e-9 0 84e-9 1e8 0
Pisection 1e8 0.7e-9 0 120e-9 1e8 0
RLseries 0 60e-9
variable R2 Decay-model
1e6 0 1300e-9 1E-9
Rcground 0

! PFL
Rcground 1070
Trline Linear 11e-9 2.65
Trline Linear 6e-9 1.61
Trline Linear 35e-9 1.3
UFO Vout
$ PFLVolts
Trline Linear 6e-9 1.7
Rcground 1070

! PFL switch
Adder
Top-Branch

Branch
Rcground 1e6 6.5e-9
RLseries 0 60e-9
Variable R2 Decay-model
1e6 0.1 1677e-9 2e-9
Rcground 0 0
```

```
! First transformer

Trline Lin 7e-9 1.6
Trline Lin 21e-9 1.2
UFO Vout
$ TX1Volts
Trline Lin 7e-9 1.5
Trline Lin 7e-9 1.95

Rcground 1e6 0.2e-9

! The Pre-pulse Switch
Adder
Top-Branch

Branch
Pisection 1e6 0.4e-9 0 37e-9 0 0
Variable R2 Decay-model
1e6 0.01 1725e-9 2e-9

! Second Transformer
Trline Linear 3e-9 2
Trline Linear 3e-9 1.5
Trline Linear 7e-9 1.3

! Modifications 7-sep-94 begin here

Trline Linear 50e-9 1.15 0.83
```

```
Trline Linear 5e-9 0.75

! Radial Water Taper
Trline Linear 5e-9 0.70
Trline Linear 15e-9 0.65
Trline Linear 5e-9 0.64
Trline Linear 5e-9 0.62
Trline Linear 5.5e-9 0.72
UFO Vout
$ H20VoltMon
UFO Iout
$ H20CurMon

! Tube -- Water Flare
Trline Linear 2e-9 0.73
Trline Linear 1e-9 1.32
Trline Linear 2.5e-9 1.36
Trline Linear 1e-9 1.9
UFO Ein
$ E_Water

Trline Linear 1e-10 12.15
! Tube -- Vacuum Flare
Trline Linear 2e-10 13.67
Trline Linear 2e-10 10.15
Trline Linear 3e-10 3.15
!
! MITL
Trline Linear 1.0e-9 2
UFO Iin
$ Tube_current
UFO Vin
$ Load_voltage
Trline Exp 0.6e-9 2 8
!
! Final Feed
Trline Linear 1e-10 13.4
!
RLseries 0 16.0e-9
! Short Circuit Load
Rcground 0.00050
UFO Iin $ Load_current
UFO ER1 $ E_Dump
```

below) can be used with the Thevenin equivalent output impedance of 1 Ω as a temporal boundary condition on a subset of the complete transmission line model. Hence the current generated in the model line is the prime measure of the model's accuracy with respect to experimental current traces inferred from any downstream stations. All such voltage waveforms show that power flow always reverses during a shot, reflected from the high impedance front end of this machine. While the added inductance of the PRS load is a noticeable perturbation, on the whole the energy dumped into the large (25 nH) initial front end inductance in the first 115 ns or so sets the amount of energy available in the load. Added to this rather stiff driver behavior is the common phenomenon of insulator stack flashover as the power flow reverses, which further decouples the load from the driver. Under such conditions the use of typical experimental voltage waveforms as boundary conditions to drive various load models can be expected to be reasonably accurate and, as is clearly shown below, can in fact be effective in accounting for the experimental behavior.

A detailed accounting of the (short) Phoenix line elements in Table I.2 shows the position of

Table I.2 Phoenix Short Line Elements

Line Component	Number of 0.1 ns Elements	Impedance [Ω]	Inductance [nH]	Monitor Point
Tube Voltage Monitor	1	.56	0.056	VT
Water Flare A	20	0.55	1.10	·
Water Flare B	10	1.10	1.10	·
Water Flare C	25	1.15	2.875	·
Water Flare D	10	1.68	1.68	T C [no.10]
Plastic	1	10.8	0.108	F S
Vacuum Flare A	2	12.15	2.43	·
Vacuum Flare B	2	10.15	2.03	·
Vacuum Flare C	3	3.15	0.945	·
Const Z MITL	9	2.0	1.80	V F C [no.5]
Const Gap MITL no.1	1	2.08936	⇓	summed
Const Gap MITL no.2	1	2.36549	·	·
Const Gap MITL no.3	1	2.81632	·	·
Const Gap MITL no.4	1	3.48224	·	·
Const Gap MITL no.5	1	4.56967	·	·
Const Gap MITL no.6	1	6.68900	·	·
Const Gap MITL no.7	1	8.12275	21.094	inductance

various monitors referred to in subsequent figures and in the typical experimental dataset. Some of these values differ slightly from those quoted in Table I.1 because they were taken from earlier drawings, but the effect on predicted waveforms is not particularly significant. Thereare three common monitor stations extracted from the model as timeseries or waveforms — the tube voltage (V T) , the tube current (T C), and the vacuum feed current (V F C). The location of each monitor within a given subset of line elements is shown as well as the location of the flashover shunt (F S) at the insulator stack. In examining the probable effect of MITL losses near the PRS loads the last four "constant gap MITL" positions are equipped with Child-Langmuir shunts dependent on local voltage for their resistance and generalized to include the effect of magnetic insulation on the electron and ion currents.

B. Performance Comparison: Voltage, Current, and Short Circuit Loads

Just like any other pulser a precise knowledge of the voltage in Phoenix is valuable because the voltage and current monitors in the water (Tube V and Tube C) serve to define the energy sent downstream to the load and thus establish the energy budget for any load or MITL loss processes, including the PRS radiation. In the figures below we show a comparison between model and data for a this comparison to a single short circuit event (#1014). The calculated energy sent downstream of the insulator stack is used as a global reference trace. The flashover event is not modeled explicitly as a standard element because, while model shunts placed near the insulator transmission line element can show similar behavior, no *unique* modeling solution exists for the given data. In the following discussion the required flashover shunts for modeling a particular event are developed, but this is a case-by-case kind of thing. The insulator flashover was also treated previously using the short line model[2] discussed above, obtaining reasonably good agreement with experiment for a range of short circuit impedances and electrical lengths.

i. Marx Current (Fig. I.2)

The model captures the peak current to within 5% but introduces a slight phase shift because it fails to mimic the somewhat slower risetime phase on the Marx during the first 200 ns. A pure LC image of the Marx will not capture this kind of behavior, which may reflect the details of switching within the Marx. The timing of later features follows the data trace, but shows more reactive, oscil-

Fig I.2

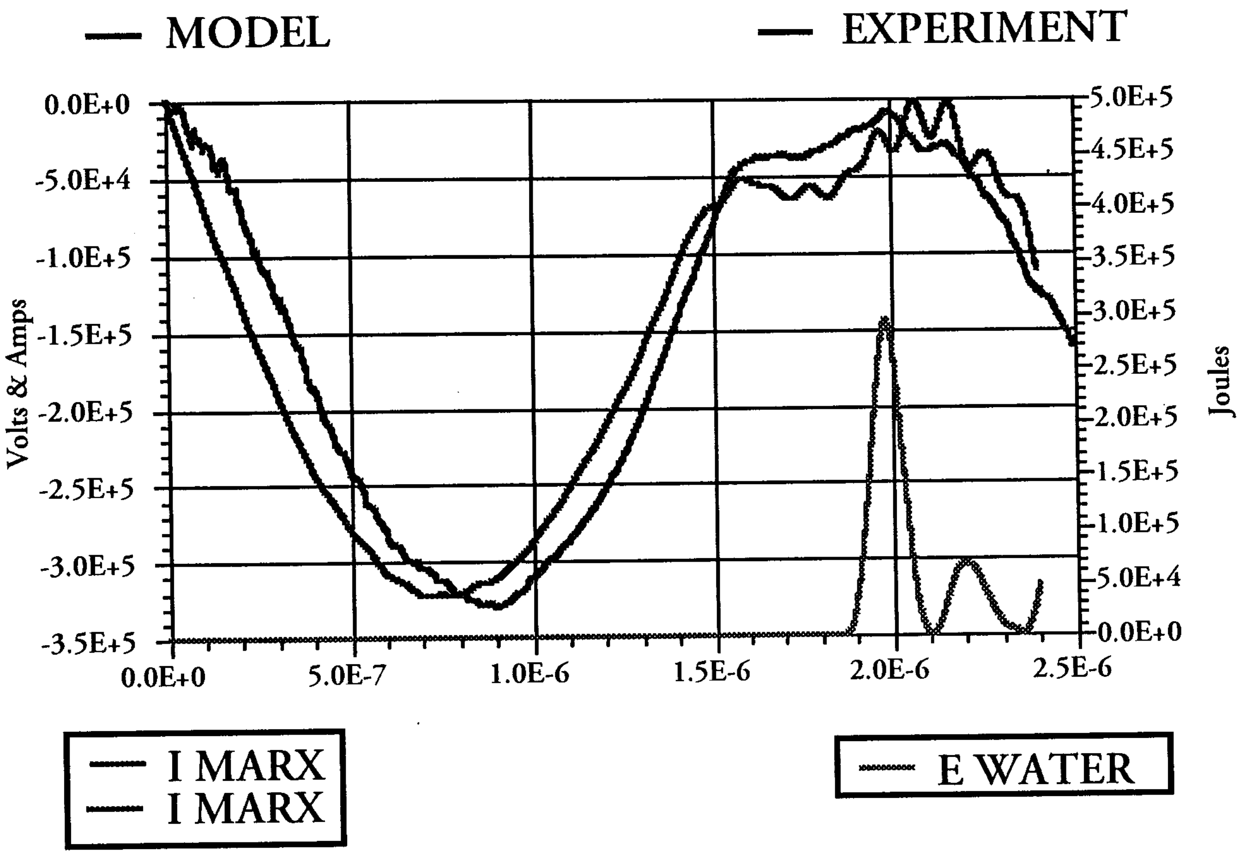
— MODEL
— EXPERIMENT
0.0E+0
-5.0E+4
-1.0E+5
-1.5E+5
-2.0E+5
-2.5E+5
-3.0E+5
-3.5E+5
Volts & Amps
5.0E+5
4.5E+5
4.0E+5
3.5E+5
3.0E+5
2.5E+5
2.0E+5
1.5E+5
1.0E+5
5.0E+4
0.0E+0
Joules
0.0E+0
5.0E-7
1.0E-6
1.5E-6
2.0E-6
2.5E-6
— I MARX
— I MARX
— E WATER

latory behavior. Again it would appear that the machine is more dissipative than the model and the (unmodeled) divertor switch probably contributes at later times ($> 2\mu s$) to this level of divergence between theory and experiment.

ii. Transfer Capacitor (Fig. I.3)

A modified model for the transfer capacitor output switch circuit was developed. It consists of a variable RL series element just prior to the voltage adder elements originally proposed. The value of series resistance must be about 1kΩ for the best fidelity to experiment — larger values fail to drain the transfer capacitor into the voltage adder, predicting too high a voltage at the TC monitor, while smaller values introduce spurious temporal variations in the signals predicted at the TC and PFL monitors. After a fixed delay, this series resistance is then set to decay on 15 ns e-folding timescale, allowing energy out of the transfer capacitor and into the voltage adder elements of the switch model.

The 1kΩ initial series resistance value used in the new model captures the peak transfer capacitor voltage to within 20% , but one can do better by lowering the local line impedance near the TC voltage monitor. A change from 2.1 Ω to 1.5 Ω gets the model and experiment to within 5 %, but such a large variation may not be justified by actual uncertainties in this impedance value. The calibration of this voltage monitor is therefore also suspect. As regards the later discharge timing features from the TC monitor data, the new model captures the major features for any of the detailed variations just discussed, but it still diverges in predicting the zero crossing at 1.7 μs. Again this may be due to actions of the divertor switch, but equally likely is the influence of the insulator flashover event, which would drive the TC monitor voltage negative sooner because of the reverse polarity pulse it must generate. Again, no *unique* modeling solution exists for the given data.

iii. Pulse Forming Line (Fig. I.4)

The modified model for the transfer capacitor output switch circuit plays an important role here, because earlier attempts proved unable to capture the PFL voltage rise hold off that is shown in the first 1.3 μs of the data trace. Since an accurate picture of the pre-pulse is of central interest in understanding the gas puff PRS initiation dynamics, the long ramp on the PFL voltage, which appeared in

Fig I.3

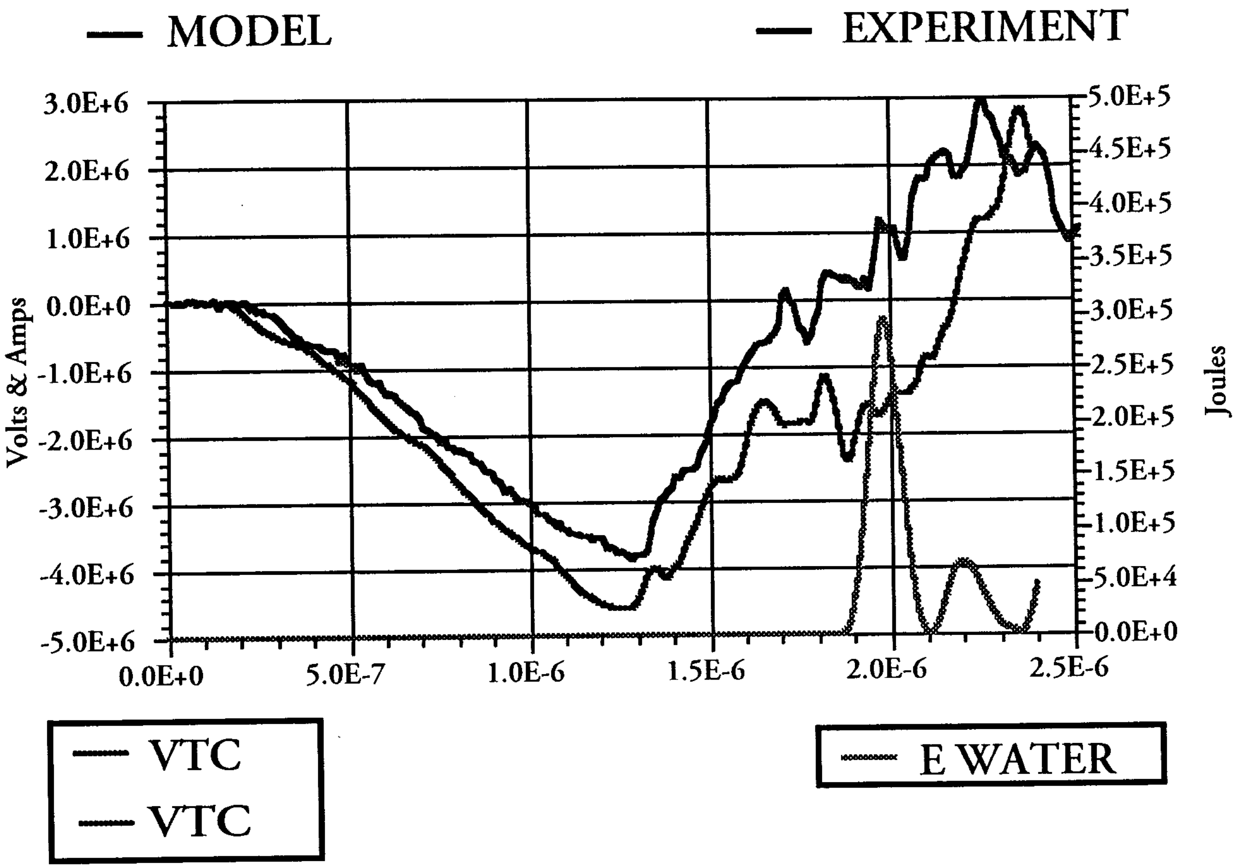
— MODEL
— EXPERIMENT
Volts & Amps
3.0E+6
2.0E+6
1.0E+6
0.0E+0
-1.0E+6
-2.0E+6
-3.0E+6
-4.0E+6
-5.0E+6
0.0E+0
5.0E-7
1.0E-6
1.5E-6
2.0E-6
2.5E-6
Joules
5.0E+5
4.5E+5
4.0E+5
3.5E+5
3.0E+5
2.5E+5
2.0E+5
1.5E+5
1.0E+5
5.0E+4
0.0E+0
— VTC
— VTC
— E WATER

Fig I.4

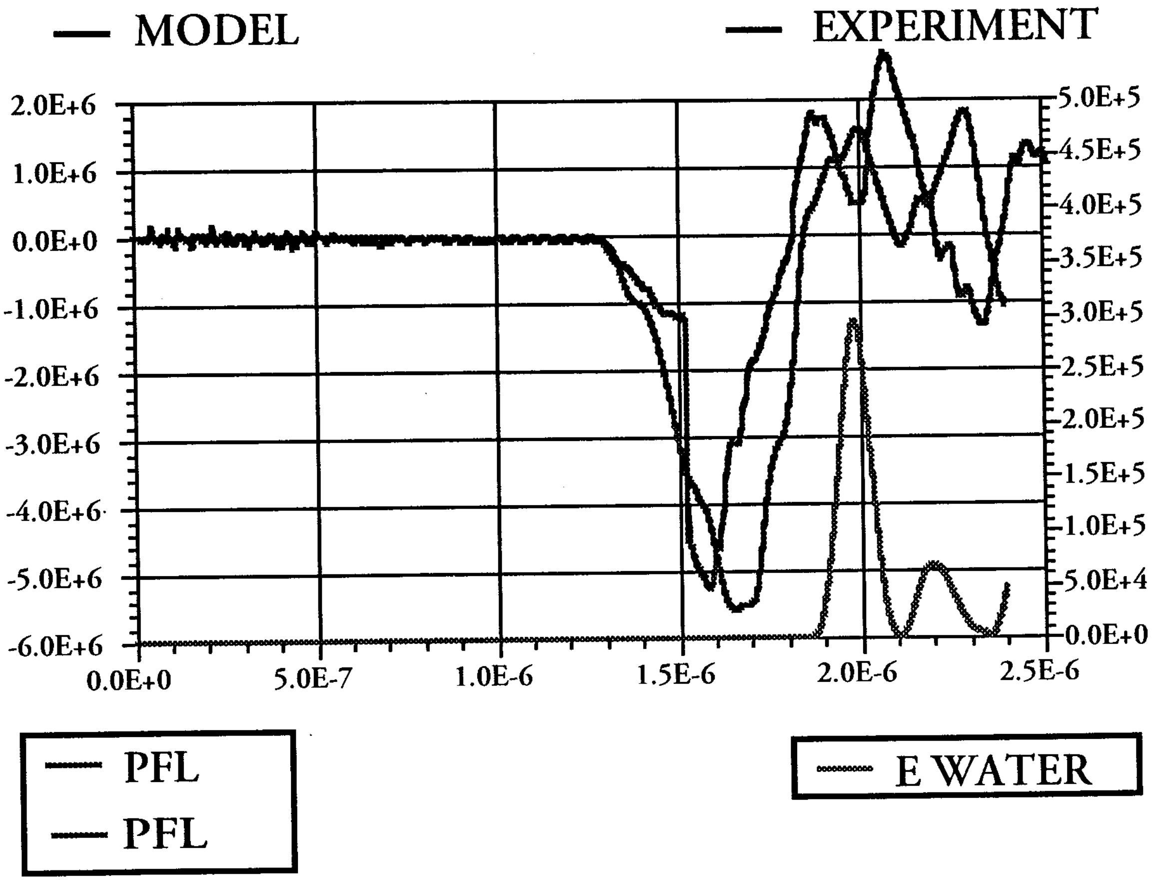
— MODEL
— EXPERIMENT
2.0E+6
1.0E+6
0.0E+0
-1.0E+6
-2.0E+6
-3.0E+6
-4.0E+6
-5.0E+6
-6.0E+6
5.0E+5
4.5E+5
4.0E+5
3.5E+5
3.0E+5
2.5E+5
2.0E+5
1.5E+5
1.0E+5
5.0E+4
0.0E+0
0.0E+0
5.0E-7
1.0E-6
1.5E-6
2.0E-6
2.5E-6
— PFL
— PFL
— E WATER

calculations with the original TC switch model, was unacceptable. The improved model removes this erroneous foot on the PFL voltage waveform; it also captures the peak voltage and first zero crossing. The PFL voltage waveform is quite insensitive to the assumptions about line impedance made in the TC stage and in the TC switch model, as discussed above. As a further check on the sensitivity of model, a comparison of the energy thrown forward of the water with changes in the line impedance at the TC monitor showed that the first energy pulse (at 2.0 μs) is unchanged, while the second (at 2.2 μs) is lowered as the TC line impedance drops, indicating that it is a secondary reflection of energy. For better agreement, the model risetime in the main PFL pulse should be sharpened and the decay time reduced, but that will be left to future work due to the number of model elements involved in the synthesis of this waveform.

iv. First Transformer (Fig. I.5)

The model's signal timing conforms fairly well to the experiment until 2.0 μs when the influence of the insulator's flashover begins to be felt at the transformer monitor station. A model for the insulator breakdown — accurate in mimicing the L/R decay behavior seen in the VFC and MITL current monitors, and also in halving the signal magnitude on the water voltage monitor — can be added to the line, c.f. our Water Monitors discussion below. When the same case is then recalculated, this first transformer signal (TX1) is strongly modified on the 2.0 → 2.2 μs time domain. The dip to zero shown here is then erased and the magnitude of the double peak feature in this voltage is reduced.

Timing considerations aside however, the model's value for the initial voltage peak is significantly larger than the measurement — the figure reflects an amplification of the voltage data by a factor of about 3.5 to bring the observation into rough congruence with the calculation. Such behavior is indicative of a need for recalibration. The general model agreement with currents and voltages both upstream and downstream of this particular monitor would not be possible if this monitor's signal amplitude were taken at face value.

v. Water Monitors (Fig. I.6a,b)

(a.) The calculated voltage waveform tracks accurately in time with the observed signal, but

Fig I.5

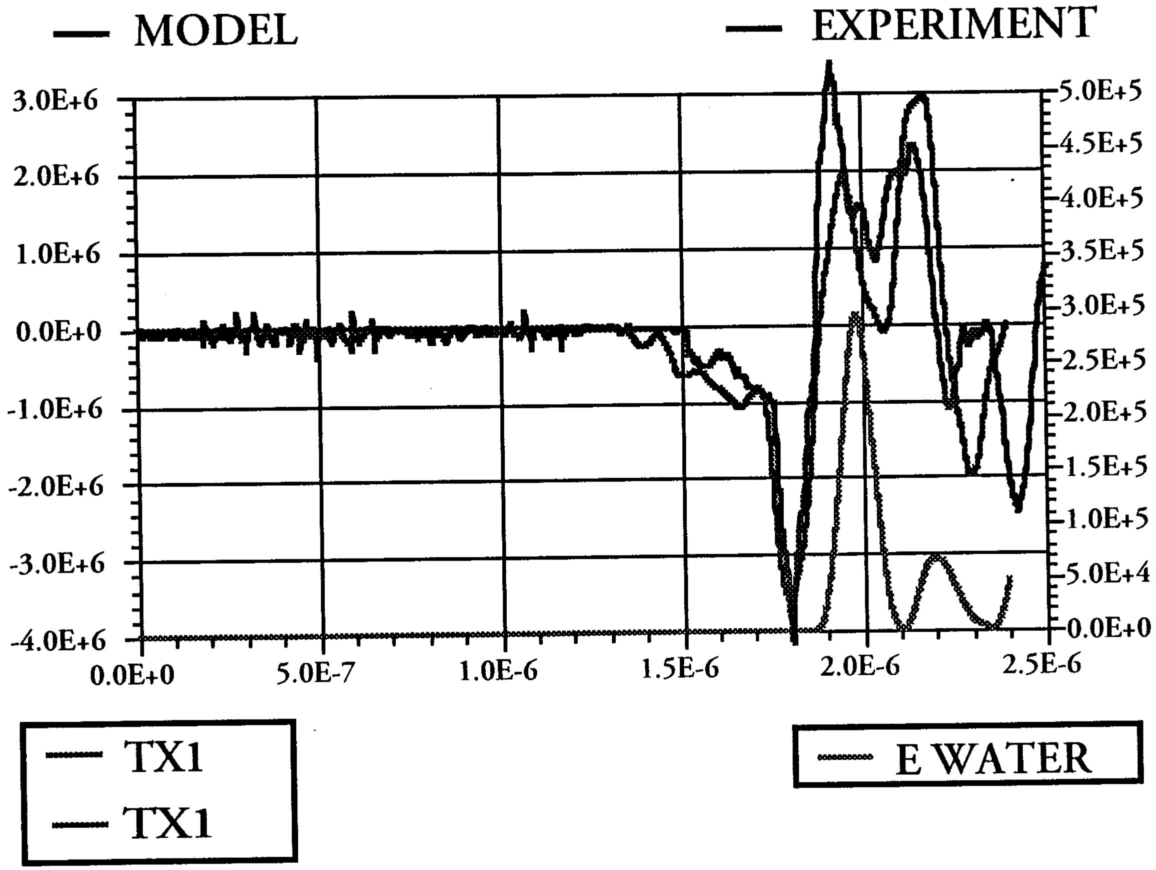
— MODEL
— EXPERIMENT
3.0E+6
2.0E+6
1.0E+6
0.0E+0
-1.0E+6
-2.0E+6
-3.0E+6
-4.0E+6
5.0E+5
4.5E+5
4.0E+5
3.5E+5
3.0E+5
2.5E+5
2.0E+5
1.5E+5
1.0E+5
5.0E+4
0.0E+0
0.0E+0
5.0E-7
1.0E-6
1.5E-6
2.0E-6
2.5E-6
— TX1
— TX1
— E WATER

Fig I.6a

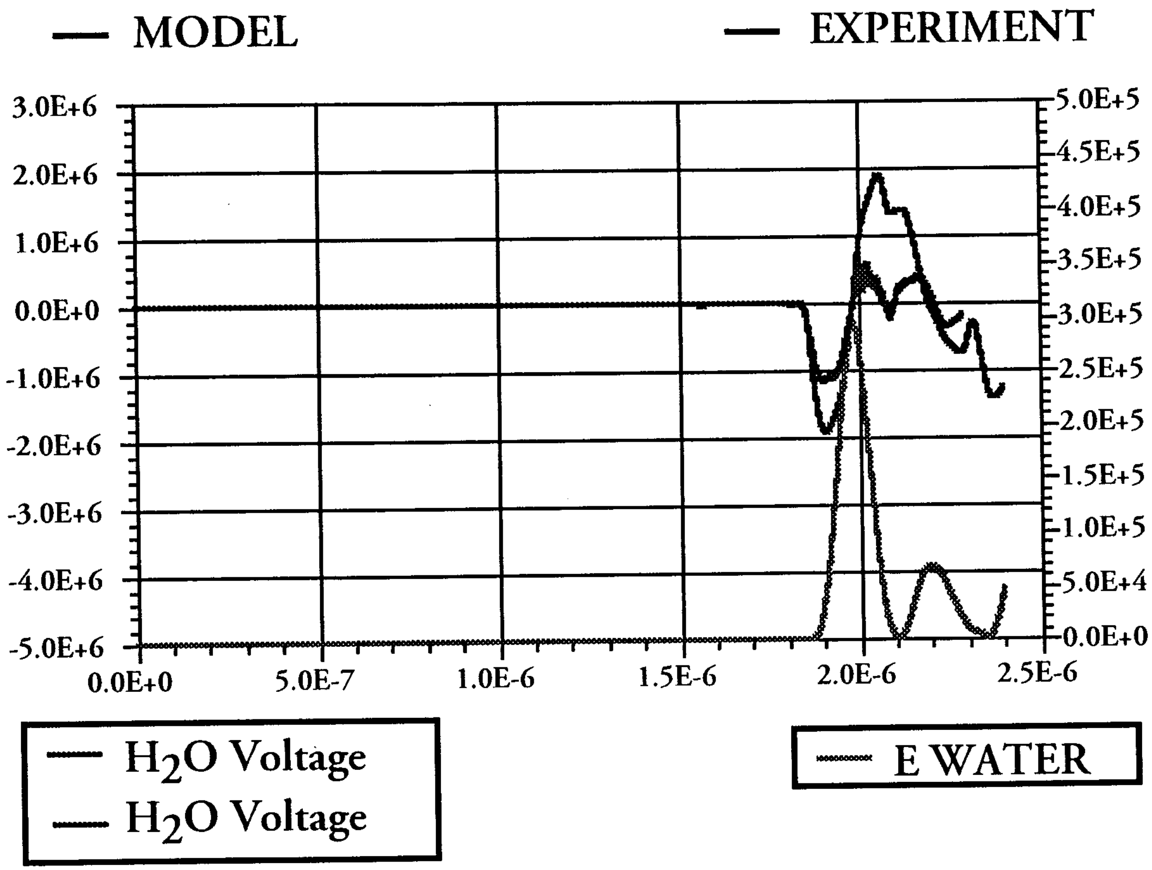

— MODEL
— EXPERIMENT
3.0E+6
2.0E+6
1.0E+6
0.0E+0
-1.0E+6
-2.0E+6
-3.0E+6
-4.0E+6
-5.0E+6
5.0E+5
4.5E+5
4.0E+5
3.5E+5
3.0E+5
2.5E+5
2.0E+5
1.5E+5
1.0E+5
5.0E+4
0.0E+0
0.0E+0
5.0E-7
1.0E-6
1.5E-6
2.0E-6
2.5E-6
— H_2O Voltage
— H_2O Voltage
— E WATER

Fig I.6b

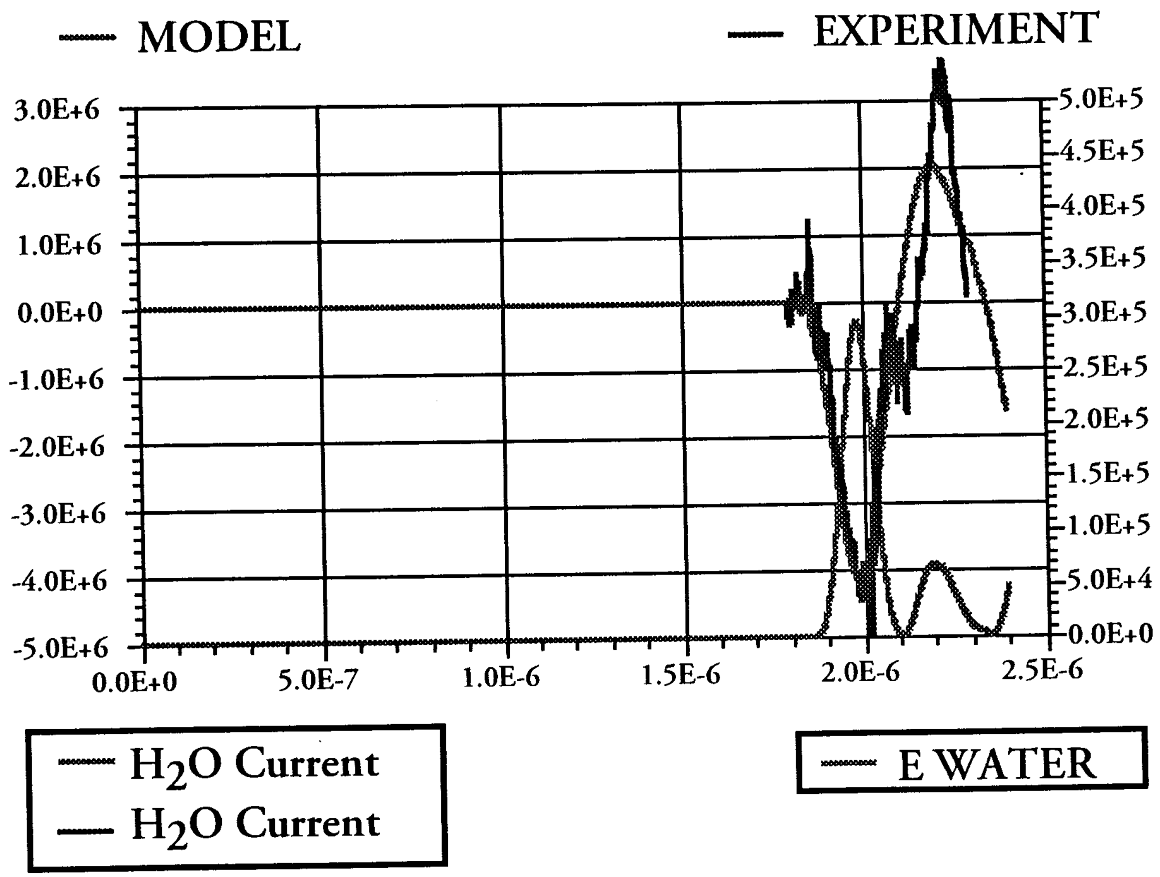

MODEL
EXPERIMENT
3.0E+6
2.0E+6
1.0E+6
0.0E+0
-1.0E+6
-2.0E+6
-3.0E+6
-4.0E+6
-5.0E+6
0.0E+0
5.0E-7
1.0E-6
1.5E-6
2.0E-6
2.5E-6
5.0E+5
4.5E+5
4.0E+5
3.5E+5
3.0E+5
2.5E+5
2.0E+5
1.5E+5
1.0E+5
5.0E+4
0.0E+0
H_2O Current
H_2O Current
E WATER

the measured voltage is lower than expected. Either the premature flashover event diminished the signal or the water monitor also needs recalibration. If one adopts a simple model of the insulator breakdown, constructed by placing a time sensitive shunt at the location of the insulator, then the choice of final impedance for this shunt determines the relative attenuation of the computed signal at the water monitor which is a few nanoseconds upstream. It is found that the observed voltage signal amplitude can be reproduced by a shunt value at the insulator of about half the local line impedance near the voltage monitor ($\approx 0.375\ \Omega$). Further, the observations require a second, parallel shunt to be triggered also, about 200ns later than the first. The second shunt lowers the impedance further and can be made to track the L/R decay that is seen as the insulator breakdown essentially crowbars the front end.

(b.) The water monitor current level is predicted fairly well whether or not the sequential shunts are used. With or without them, and for mild variations in the shunt impedance, one finds that peak current values at the water monitor are still captured at about 4 MA. This insensitivity to impedance value is absent in the choice for timing the sequential breakdowns. Here, in contrast, good timing is critical to modeling the event. The most accurate timing choice is to bring these shunts into play coincident with two clear spikes in the observed water monitor current waveform that are separated by about 200 ns.

vi. Vacuum Feed (Fig. I.7)

When the breakdown model is absent, the predicted current tracks the experiment precisely (2.9 MA in 90 ns) until the flashover event. Adding the shunts to mimic the flashover then forces the model current into an exponential decay that is essentially the same as the observed waveforms, but the modeling solution is hardly unique. The shunts are constrained by the observations given to occur a particular times, and to provide resistive paths on the order of a few hundred milli-Ohms, but the details of their placement in the line and their decay history are not determined.

If a complete picture of the flashover event generated by this model is assembled, then the model is seen to move "closer" to the experiment in the four interdependent waveform features just discussed. The results to date clearly indicate that (i) the current limitations seen in the shot are indeed due to an insulator flashover, and (ii) the model is capturing at least the gross features of the

Fig I.7

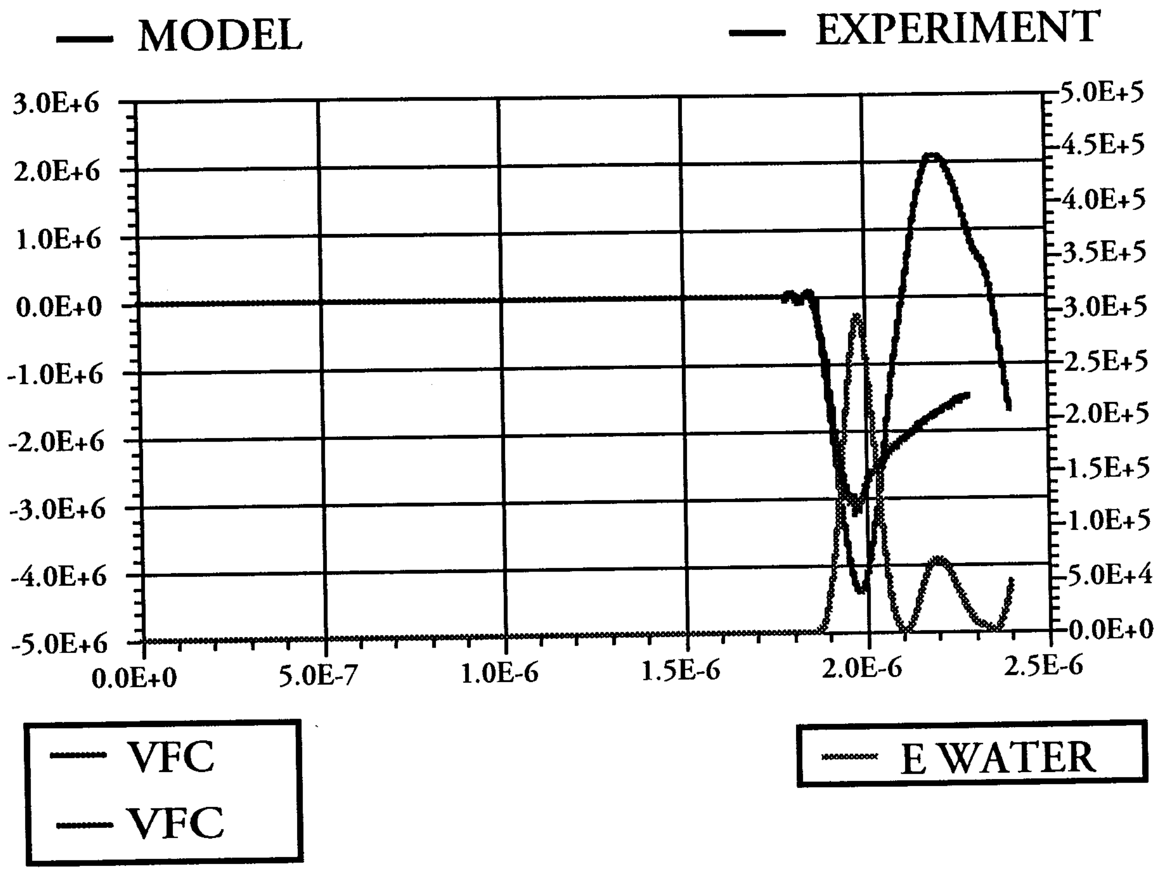
— MODEL
— EXPERIMENT
3.0E+6
2.0E+6
1.0E+6
0.0E+0
-1.0E+6
-2.0E+6
-3.0E+6
-4.0E+6
-5.0E+6
5.0E+5
4.5E+5
4.0E+5
3.5E+5
3.0E+5
2.5E+5
2.0E+5
1.5E+5
1.0E+5
5.0E+4
0.0E+0
0.0E+0
5.0E-7
1.0E-6
1.5E-6
2.0E-6
2.5E-6
VFC
VFC
E WATER

insulator breakdown observed.

C. Equivalent Circuit

As a simplifying strategy in examining the operation of any PRS driver the equivalent circuit is often used. Consisting of a voltage waveform that is a specified function of time and an output impedance that is fixed in time, the equivalent circuit can approximate the load coupling behavior of the full pulseline, even when driving a variable impedance load that mimics a PRS. Encapsulating the complexities of the driver into a simple pair of circuit elements, the modeling effort devoted to the PRS itself can proceed more quickly.

On the other hand there is a modest price to pay for the slick versatility of the equivalent circuit — the energy delivery error (inherent in the approximation) is not constant over the domain of load impedances, it will increase as the load impedance moves above or below the matchpoint. In PRS studies this behavior can be compensated for by "overvolting" the equivalent circuit to make up for the energy error and by restricting the load impedance domain considered. Once anything more ambitious than a scoping study is desired a full model of the driver should be employed, usually at only a moderate increase in computing cost.

i. Baseline impedance study

Since PRS modeling concerns itself with computing the yields and power levels expected in cold X-ray bands, a central requirement for a successful computation is the energy input from the pulseline driver. To this end the equivalent circuit derived here varies slightly from the usual prescription that is obtained by (i) constructing the *time varying* ratio of open circuit voltage to short circuit current and (ii) selecting the output impedance as the minimum of the resulting waveform over the time domain.

Here a sequence of calculations of energy coupling to a fixed resistive load at the location of the PRS is used to determine the best match in load impedance. In effect the load impedance is optimized until only a forward wave exits the pulseline to be absorbed in the load. In Phoenix all the real loads explored in the laboratory exhibit a fairly substantial amount of reflected power, but for impedances in the $0.9 \rightarrow 1.0\ \Omega$ range the usual voltage reversal after peak current is minimized.

At such an impedance the Phoenix line would transfer about 800 kJ of energy to a fixed load. One such calculation for a low load impedance is shown in (Fig. I.8) — a QuickTime movie of all such calculations shows that the energy transfer is greatest and the reflected power is least for the 1.0 Ω case.

ii. V_{mon} from the matchpoint

A subsequent drawing (Fig. I.9) shows the voltage waveform computed at the location of the waterline monitor at the best impedance match. A polynomial fit is also shown, which will provide a simple driver source term for the equivalent circuit. In practice an equally useful input can be formed by a voltage table, depending upon the input stream preferred by the PRS model.

At this level of approximation the location of the monitor voltage and the insulator stack are viewed as coincident. So our equivalent circuit model of the machine elements upstream of the water voltage monitor must be chosen so as to deliver the expected energy past the water monitor and water-vacuum interface.

iii. Thevenin equivalent circuit

Putting the pieces together results in the circuit diagram shown (Fig. I.10) with an output impedance of 1.0 Ω for the pulseline as a whole. The lumped inductance downstream of the insulator stack is shown as a fixed inductive load, to which is added the variable inductance of the imploding PRS. The proper driver voltage at the source element is twice the observed monitor (or insulator) voltage because at the match point one must divide the source voltage exactly by two to get the observed monitor signal from the complete model. A calibration coefficient is shown to normalize the driver voltage to the initial charge on the Marx bank.

iv. Equivalent circuit performance

The next series of figures show some results that check the equivalent circuit. First, use the equivalent circuit to drive a foreshortened but *otherwise complete* line model that begins at the waterline voltage monitor and terminates with the matching impedance. The equivalent circuit indeed delivers at the voltage monitor a time dependent signal that precisely mimics the driver waveform and displays an amplitude peak half that of the driver. The energy delivered to the matched load

Fig I.8

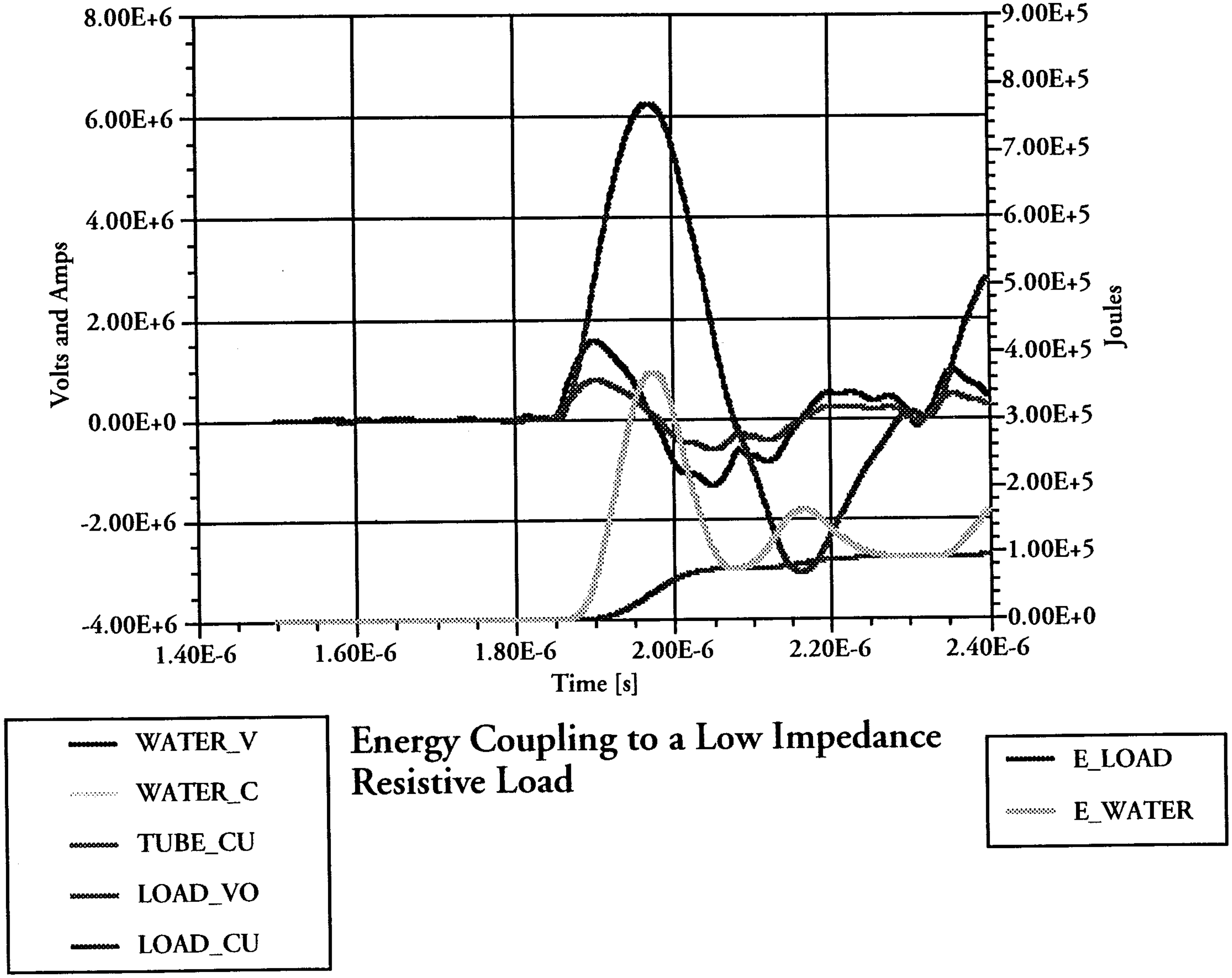
8.00E+6
6.00E+6
4.00E+6
2.00E+6
0.00E+0
-2.00E+6
-4.00E+6
Volts and Amps
9.00E+5
8.00E+5
7.00E+5
6.00E+5
5.00E+5
4.00E+5
3.00E+5
2.00E+5
1.00E+5
0.00E+0
Joules
1.40E-6
1.60E-6
1.80E-6
2.00E-6
2.20E-6
2.40E-6
Time [s]
WATER_V
WATER_C
TUBE_CU
LOAD_VO
LOAD_CU
Energy Coupling to a Low Impedance Resistive Load
E_LOAD
E_WATER

Fig I.9

Fit to Screamer open circuit voltage for Phoenix. Use with the furnished equivalent circuit as Vin=2•Vmon(t)•[Vcharge/87kV], where Vcharge is the initial Marx charge voltage.

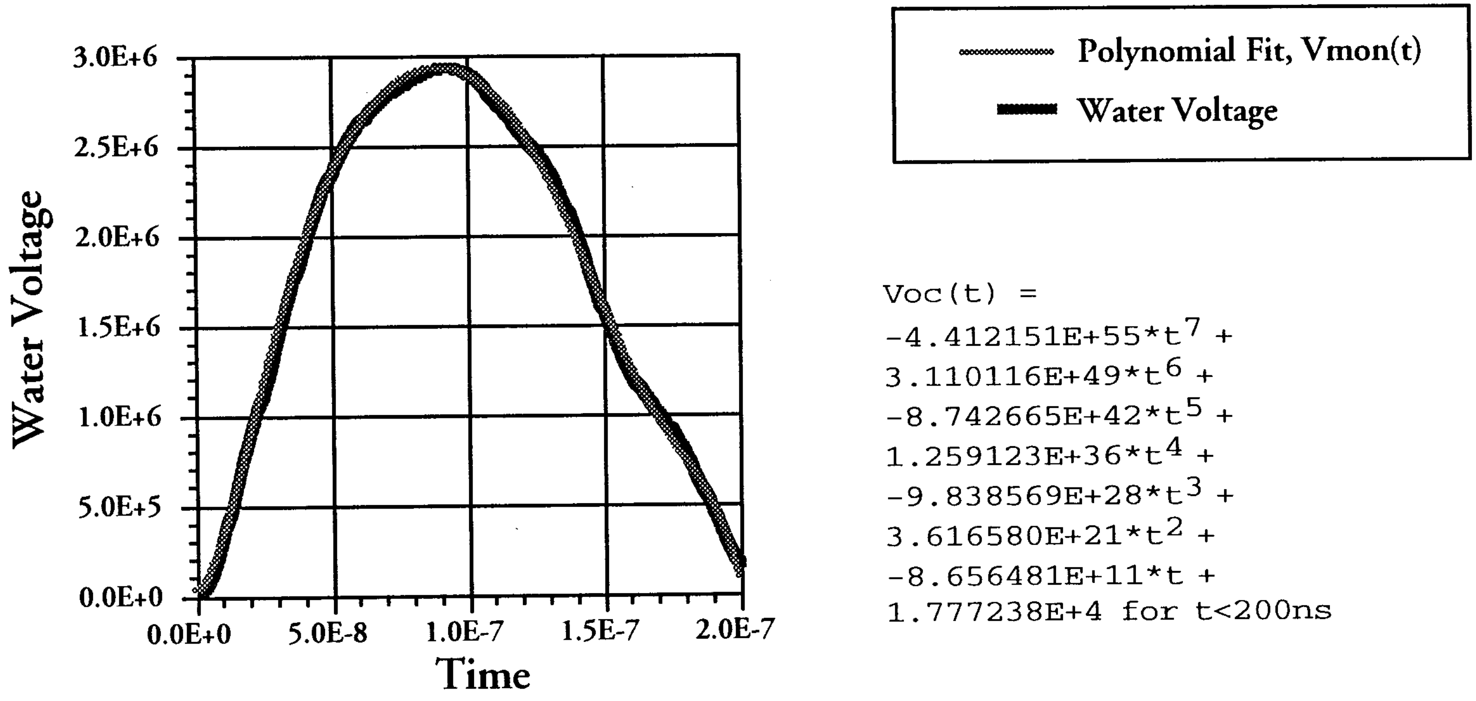

$$
\begin{aligned}
&Voc(t) = \\
&-4.412151E{+}55*t^{7} + \\
&3.110116E{+}49*t^{6} + \\
&-8.742665E{+}42*t^{5} + \\
&1.259123E{+}36*t^{4} + \\
&-9.838569E{+}28*t^{3} + \\
&3.616580E{+}21*t^{2} + \\
&-8.656481E{+}11*t + \\
&1.777238E{+}4 \text{ for } t<200ns
\end{aligned}
$$

Fig I.10

PHOENIX: EQUIVALENT CIRCUIT

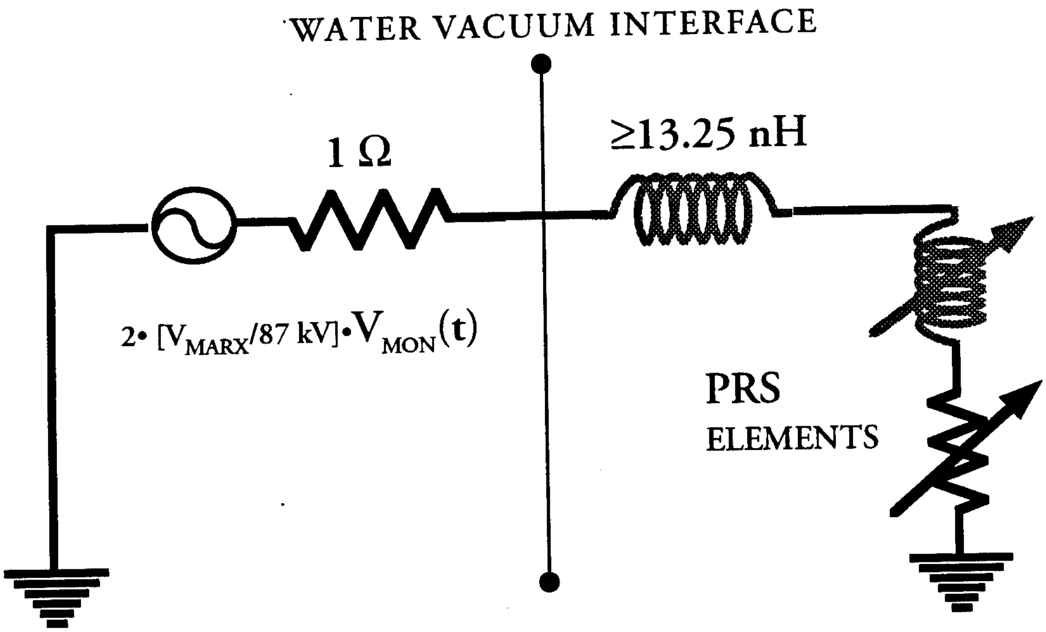

is precisely the 800 kJ expected from the very nature of the equivalent circuit construction, (Fig. I.11).

Next, keep the line model details and the equivalent circuit driver, but lower the terminating impedance to 0.2 mΩ and, as shown, the peak delivered energy becomes about 250 kJ. The full model into such a load would deliver about 300 kJ, illustrating the systematic error inherent in loading an equivalent circuit rather than a "real" circuit, (Fig. I.12).

Finally, lump the downstream inductance into a single element and use the equivalent circuit driver, keeping the same termination. The peak energy delivery now drops to about 200 kJ, (Fig. I.13).

The three figures therefore show that as one gets less careful about the line model, on the low impedance side of the match point, the estimate of energy transfer to the front end inductance degrades in precision by about 33%.

D. PRS Models

In the present context the PRS model available in the Screamer code shall be the basis for comparisons among various mass loadings and power flow events or modifications. This particular PRS model is quite primitive, even for a 0D formulation, but it is equipped with a general scaling rule for PRS output which distills many years of effort into a relatively straightforward calculation. On the basis of accumulated kinetic energy in an imploded slug of material of specified mass and length, the expected yield from any of several commonly used atomic species is computed over the active rundown time.

Active rundown time is determined by the selection of a minimum radius R_f for the implosion. The common choice to measure kinetic energy delivery at a fixed fraction of the initial radius is modified here. The kinetic energy coupling generally tracks the change in inductance produced in the load, but that inductance change is fixed if the implosion is followed only to a constant fraction of R_o. By having the slug model (implicitly) undergo transition from an annulus to a cylinder at a prescribed lower radius rather than at a prescribed fraction of the initial radius, this final stagnation radius is a fair measure of the change in inductance achieved and can be explicitly tied to experi-

Fig I.11

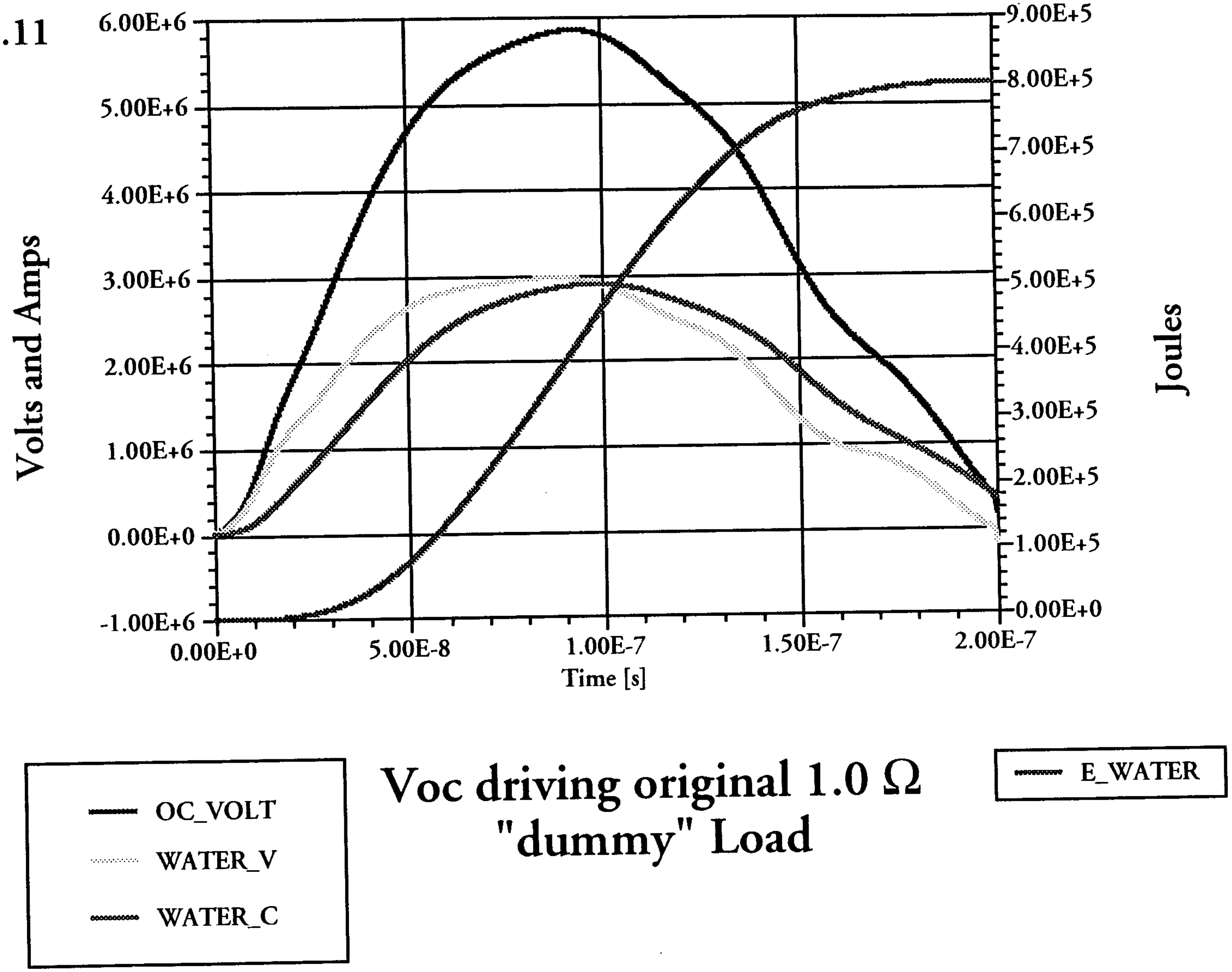

Voc driving original 1.0 Ω "dummy" Load

Fig I.12

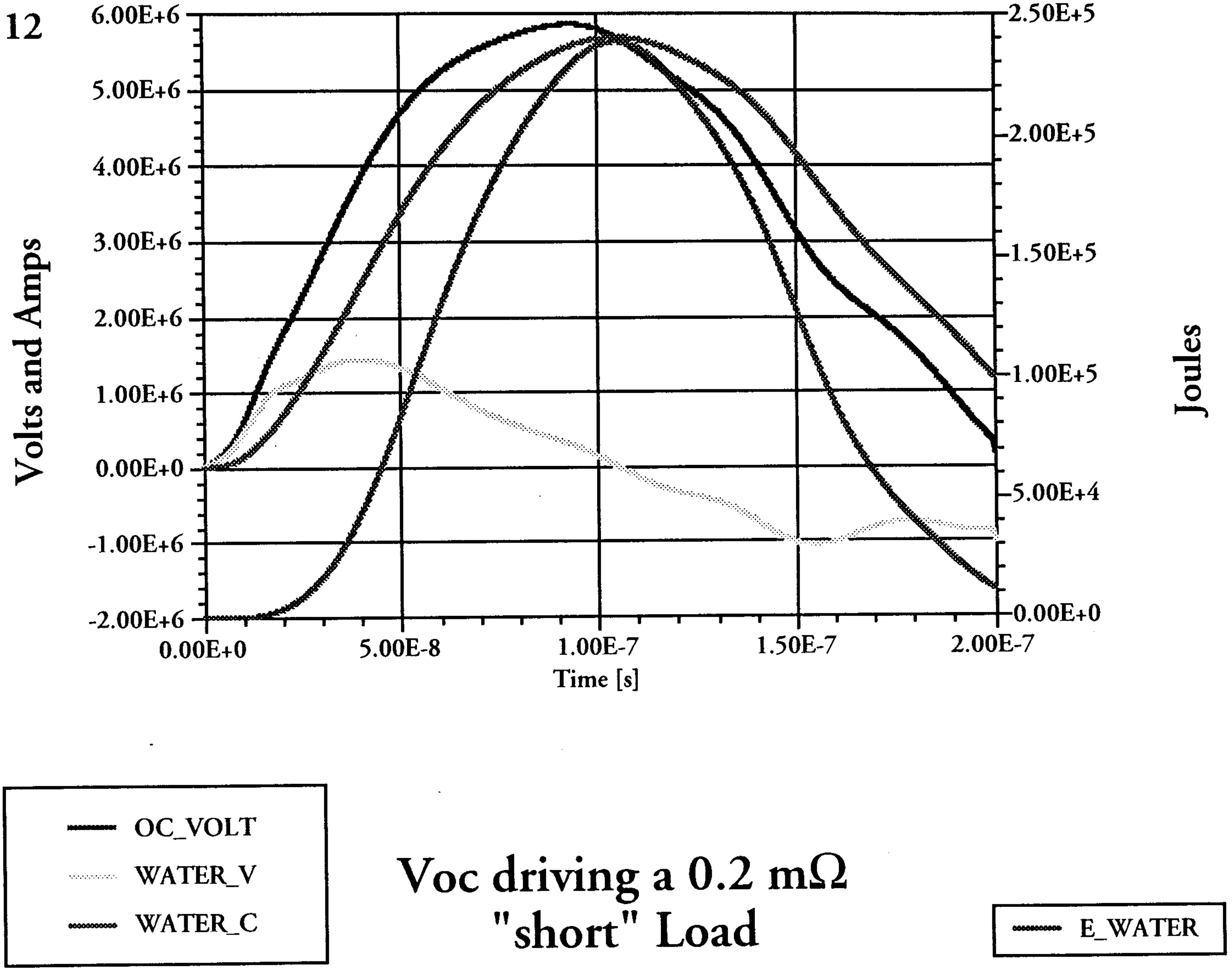

Voc driving a 0.2 mΩ "short" Load

Fig I.13

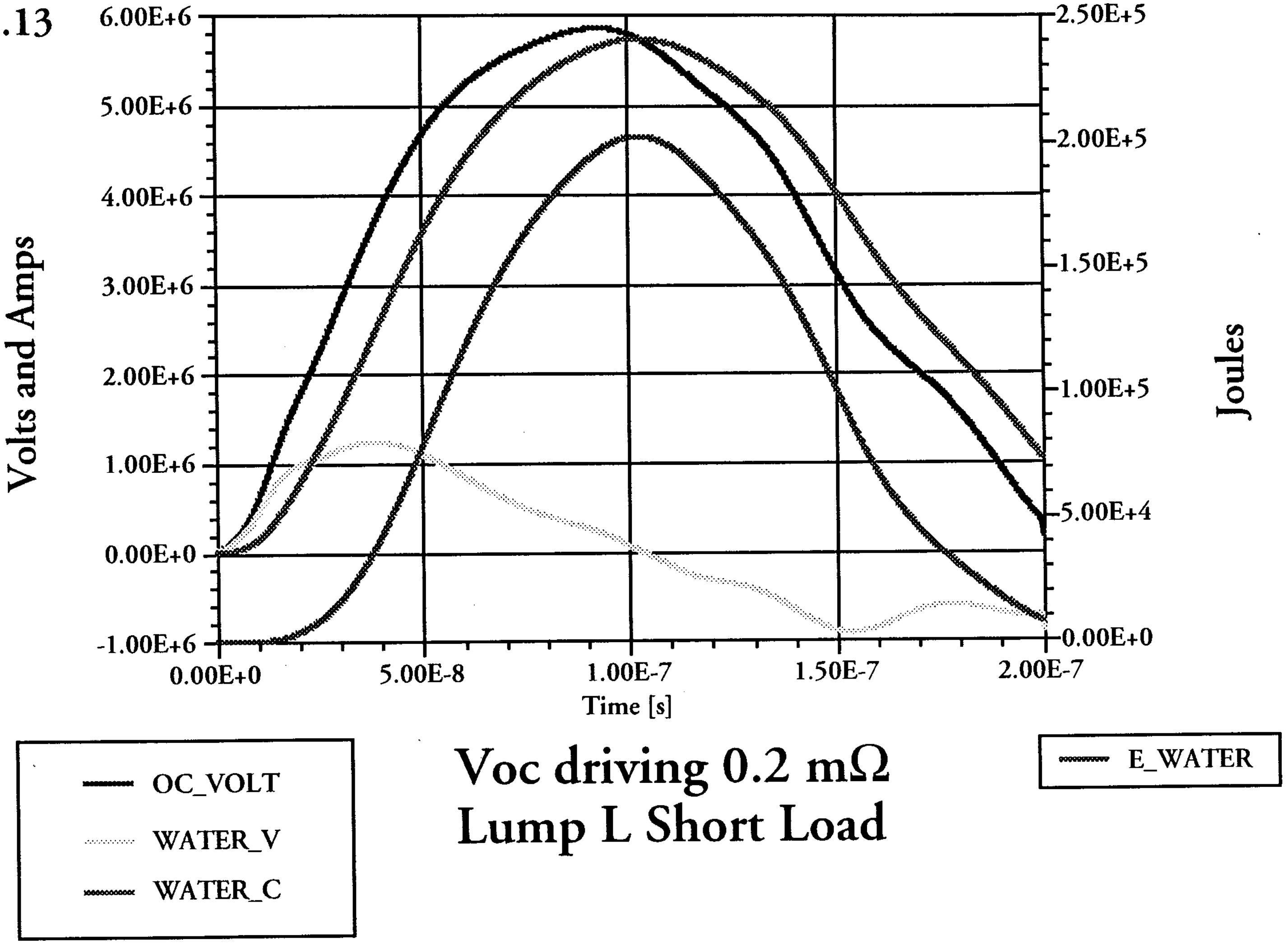

Voc driving 0.2 mΩ
Lump L Short Load

mental observations. The peak load kinetic energy is therefore recorded at this time of assembly, and is then used to compute the expected yield. Therefore, by selecting absolute values of initial and final radius, a coupling study can get a clearer picture of the correlation between inductance change and kinetic energy delivery.

i. Full Line and Slug Load

As a baseline PRS calculation, take: the initial Marx charge at V_{Marx} = 70 kV; the initial radius equal to that of the existing gas puff hardware at R_o=1.75 cm; the pinch length at a value about midway through the allowed range, viz. ℓ_{pinch}=3.0 cm; the initial mass as that inferred from measurements [3] of the neutral flow pattern, m_o=360.0 μg; and the final radius R_f=2.50 mm, compatible with the observed accumulation radius on pinhole camera diagnostics of the Phoenix PRS.

For ideal driver and puff operation such a load would be expected to produce about 12 kJ of Ar K-shell radiation, as shown in Fig. I.14. The peak current should approach 5 MA just before implosion, and about 250 kJ of energy should be coupled to the Phoenix diode by the time the load stagnates with about 110 kJ of kinetic energy. The water voltage monitor would expect a peak signal of about 2.6 MV, while the load region expectation would be a nearly 4 MV peak.

Such large voltage loadings might raise the suspicion that failures of magnetic insulation would be a source of energy loss to the Phoenix PRS. It is easy to check this conjecture by developing a simple measure of the probable quality of magnetic insulation under these idealized Phoenix load conditions. The critical current for magnetic insulation can be written[4], with $\epsilon = \frac{eV}{m_0c^2}$ as,

$$I_c = I_\alpha g \sqrt{\epsilon(\epsilon+2)} \qquad (I.1)$$

with Creedons parameter I_α ≈8.5 kA. For the Phoenix line at a feed radius r_0=10 cm, and a gap d of 1 cm, the geometric factor $g \equiv 1/\ln(1+d/r_0)$ becomes 10.5. Combining the leading factors yields

$$I_c = 345\sqrt{\frac{\epsilon(\epsilon+2)}{15}}\ [kA] \qquad (I.2)$$

Fig I.14

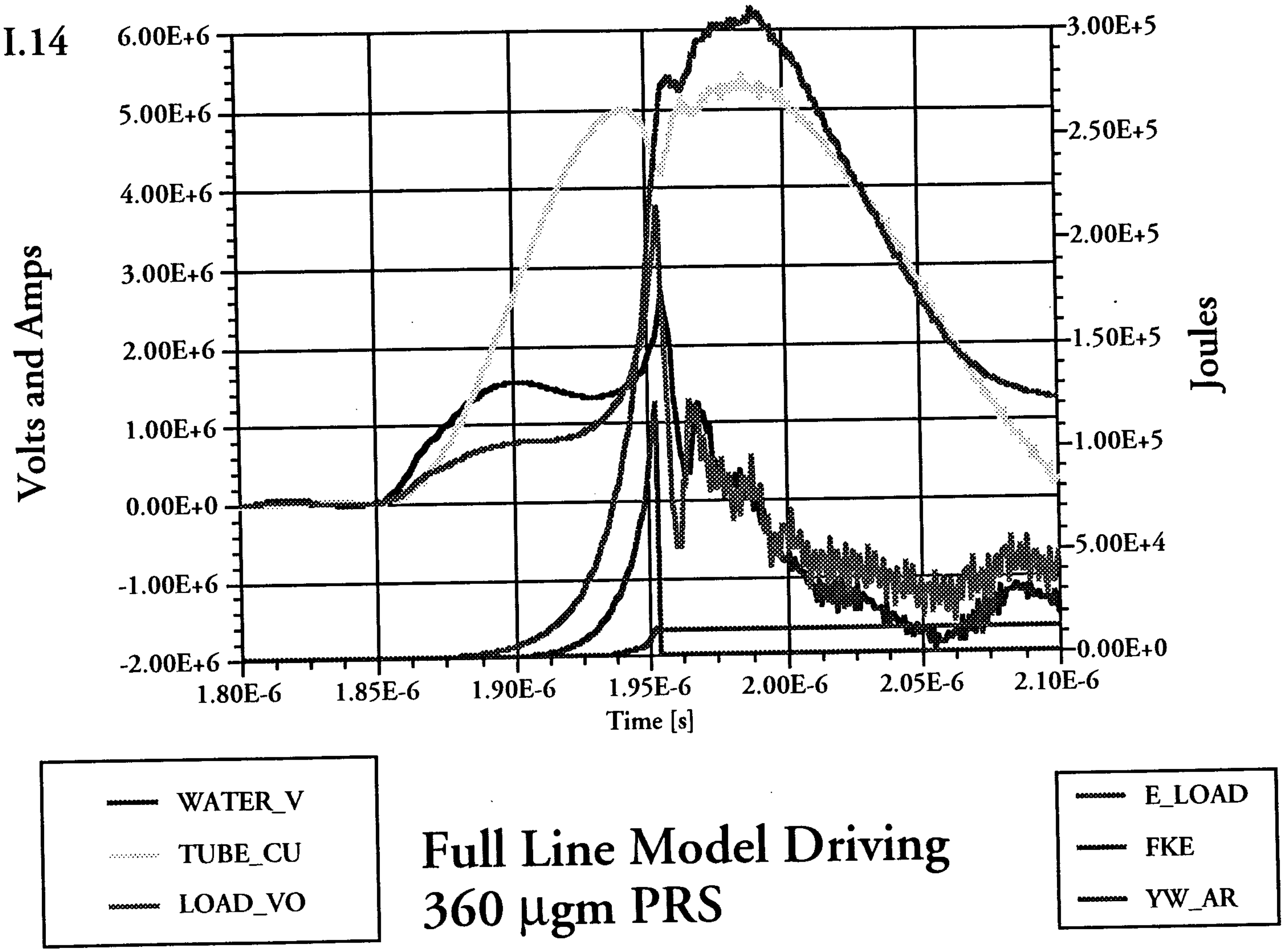

Full Line Model Driving
360 µgm PRS

in the front end of Phoenix. Therefore Phoenix voltage loadings, like the peak of 4 MV estimated above, would imply a critical current of about 780 kA. When compared with an expected current of about 4 MA, the ratio I/I_c=5 would imply rather good magnetic insulation in the load region. Conditions at larger radii back near the insulator stack may not be so favorable, and the insulator stack itself may be a source of fairly complex emission patterns, indicating a need for further detailed treatment.

ii. V$_{oc}$(t), Short Line and Slug Load

When the same case is calculated (Fig. I.15) using the equivalent circuit driver discussed above, the most pronounced degradation is seen in the expected energy delivery, but it occurs mostly in the later portion of the pulse. The net result at implosion time is a fairly small change in the load current, a more modest change in the peak load voltage, but very little change in the expected kinetic energy and, hence, in the expected yield.

iii. Good Al and Ar Slug Loads — K.E.(m_o, R_o)

The following table shows the peak stagnation kinetic energy (KE) at the time the load intercepts the fixed minimum radius (of 2.5 mm). The standard mass loading at 120 μg/cm for a 3 cm long wire array is appropriate for Aluminum wire loads, and appears in boldface at the (2,2) position in the table.

Table I.3 Phoenix Energy Coupling for Wire Style 3 cm Load

Peak KE [kJ]	$m_oR_o^2$	[mg cm^2]	⇒	
⇓ Radius [cm]	0.8820	1.1025	1.3230	1.5435
1.3125	61.778	64.223	64.260	66.661
1.7500	69.579	**71.298**	77.777	79.397
2.6250	79.706	91.760	86.942	87.812
3.5000	94.224	91.759	99.199	98.702

The next table shows the peak stagnation kinetic energy (KE) at the time the load intercepts the fixed minimum radius (of 2.5 mm). The standard mass loading at 90 μg/cm for a 4 cm long pinch is appropriate for Argon gas puff loads, and appears in boldface at the (2,3) position in the table.

Fig I.15

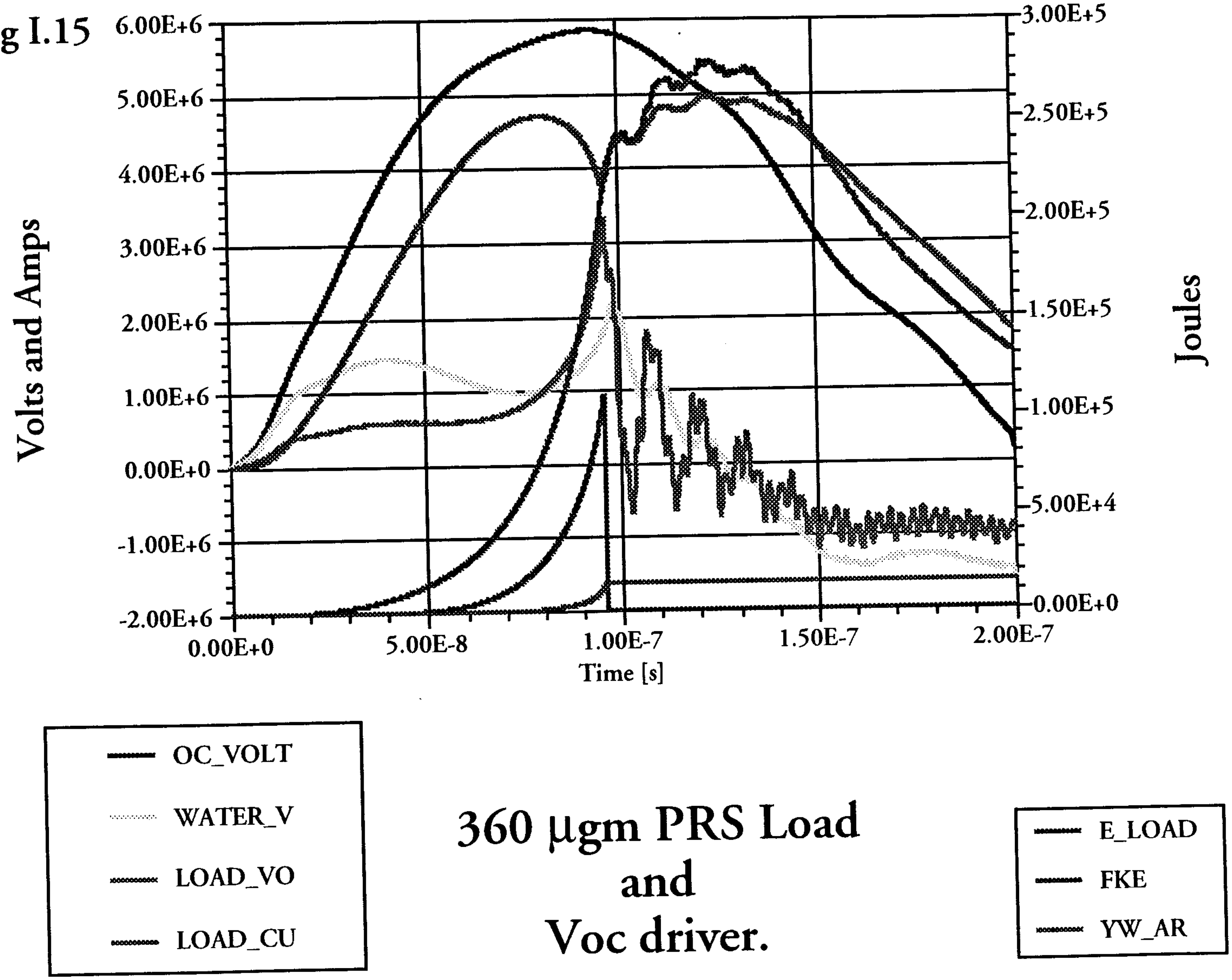
360 μgm PRS Load and Voc driver.

Table I.4 Phoenix Energy Coupling for Puff Style 4 cm Load

Peak KE [kJ] ⇓ Radius [cm]	$m_oR_o^2$ 0.780	[mg cm^2] 1.040	⇒ 1.300	1.820
1.4250	66.137	72.407	77.798	92.445
1.9000	75.105	80.996	**96.373**	101.45
2.8500	86.951	91.857	109.81	112.62
3.8000	86.934	106.68	109.81	127.56

In both these studies it is clear that present operating points are fairly well positioned with respect to mass, operating in a domain where the accepted kinetic energy is rising slower than the mass. Thus, under these conditions, the driver is already doing about as well as it can in optimizing the kinetic energy per ion to gain access to K-shell radiation states. Both load styles would also benefit from operations at a larger initial radius, but that is constrained by stability considerations as well.

II. INITIAL POWER FLOW AND PRS BREAKDOWN

From the earliest phases of research into the possibility of using gas puff loads on Phoenix, the issue of "zippering" and how to control it was a central concern. The notion of "zippering" deals with the asynchronous implosion of different axial regions in a gas puff, often resulting in the sequential lighting along the axis of the dense k-shell emitting region of the pinch. In the strictest sense of the word, it is an effect measuring the axial "writing speed" of the radial stagnation process. In the limit of extremely fine axial synchrony, the phenomenon might even progress along the axis at superluminal speed, but in existing PRS devices no such performance has been observed.

Since gas puff nozzles exhibit a radial spreading of the flow as it exits axially, the zippering is expected to progress away from the nozzle. Gas at a more distant axial position from the nozzle has a wider radial extent and requires more time to assemble on axis. Therefore the common solution to this sort of zippering is to cant the nozzle slightly inward, converging the neutral flow radially as it exits and thus counteracting the spread. The gas Mach number and nozzle tilt angle are then the tuning parameters used to optimize the design. For Phoenix, gas nozzles were constructed with several tilt angles and this effort was guided by theoretical work with 2D MHD codes.

The nozzle design chosen was subjected to a rather precise mapping of its neutral flow pattern, as referenced above and such a map is shown in Fig. II.1 at 1.3ms after the nozzle is activated. When animated these maps show that a very complex radial stagnation and rebound arises, coupled to an axially modulated flow. The breakdown of this gas in the 20 kV RF-like prepulse from Phoenix then determines the final plasma distribution subjected to the main electrical discharge from the Phoenix line.

A "2X" pinhole camera, mapping four distinct axial pinch segments to images on four XRD detectors, was constructed to observe whatever zippering behavior might arise. The Al XRDs are equipped with 0.5 mil Kapton high pass filters to bias observation into the x-ray band $\geq$2.8 keV defining the Ar k-shell; in the absence of the pinhole all four detectors are balanced to within 5 % in their output. With the pinhole in place, the end stations see about 7.1 mm of source plasma, while the central stations see about 8.2 mm of source plasma.

Fig II.1

FIELD SOLUTION & DENSITY MAP

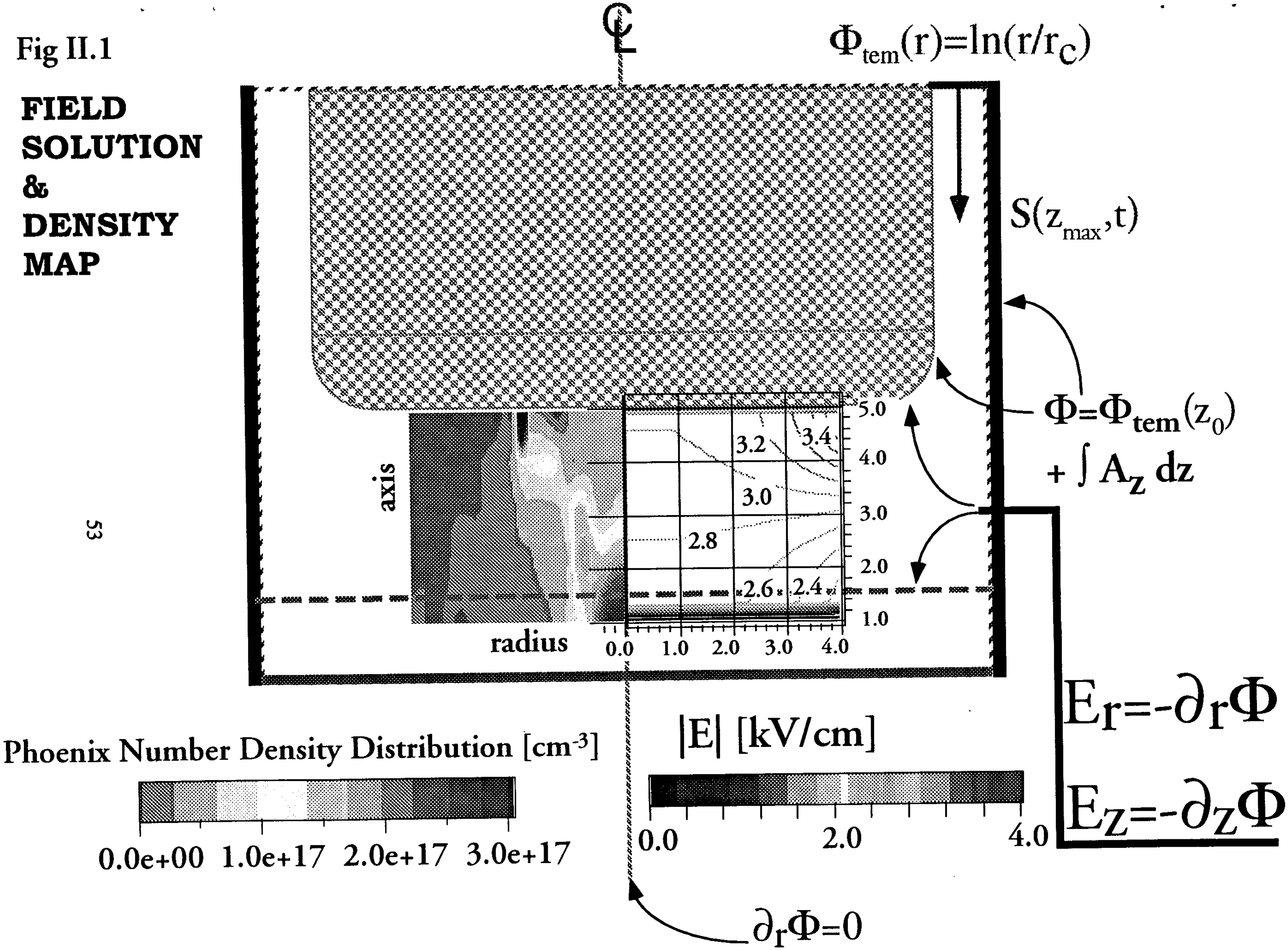

Once gas puff shots were initiated, the observed zippering behavior indicated trends in apparent opposition to conventional MHD models. The sequence of radiation is seen to vary in fairly complex patterns and the XRD stations see very broad pulse widths. Most events show a temporal sequence away from the nozzle, with some showing a sequence beginning in the middle and progressing to either end. The more effective shots tend to be those with a temporal sequence away from the nozzle.

This behavior would not be expected from the typical MHD calculation scenario wherein the model plasma mass, while matched to experimental distributions like those noted above, is set to be conducting in all locations with densities above a preset threshold. The implosion calculation from such an initial state results in "zippering" *back toward the nozzle.* In the experiment, the higher mass, larger R_o regions near the nozzle (cathode) are radiating in the Ar k-shell sooner than lower mass, smaller R_o regions near the mesh (anode).

If the topsy-turvy radiation sequence is indeed due to radial pinch kinematics, then other factors outside the scope of conventional MHD must be significant influences on the pinch motion. As a first hypothesis one may imagine that the location and early dynamics of the current channel may play an important role in accounting for this behavior. To test this idea a model for the prepulse and early Ar breakdown has been constructed. This theory has two primary elements: the field model and the ionization model; it has been developed to the extent that an initial breakdown path can be inferred for any given initial gas density map. Once a breakdown path is established the 2D MHD model can be biased to place current there and to investigate the implied consequences with respect to the XRD pinhole diagnostic array.

Field Model

The active field modes for a z-pinch PRS are the transverse magnetic (TM) modes, which can be characterized by a scalar potential (connected to the pulseline drive voltage at the inlet) and a single axial component of the vector potential (connected to the pulseline drive current at the inlet). When the conduction of the gas puff load is to be treated it is particularly convenient to work in the Lorentz (or radiation) gauge to formulate the theory. Let the axial vector potential $\mathbf{A}_z(r, z, t) =$

$a(r,z)e^{-i\omega t}\hat{z}$ and, upon adding the scalar potential $\Phi_z(r,z,t)= \phi(r,z)e^{-i\omega t}$, also with a harmonic time variation, the electric field is given by

$$\mathbf{E} = -\nabla\Phi - \frac{1}{c}\partial_t \mathbf{A}_z \, . \tag{$II.1$}$$

One then derives the coupled Helmholtz equations

$$\nabla^2 a + \frac{4\pi i\omega\sigma}{c} a + \frac{\omega^2}{c^2} a = \frac{4\pi\sigma}{c}\nabla\phi \, , \tag{$II.2$}$$

and

$$\nabla^2\phi + \frac{\omega^2}{c^2}\phi = 0 \, , \tag{$II.3$}$$

which determine all field components in the PRS cavity. Using only the complex amplitudes, the fields are derived through the relations

$$E_z = -\partial_z\phi - \frac{i\omega}{c} a \, , \tag{$II.4$}$$

$$E_r = -\partial_r\phi \, , \tag{$II.5$}$$

$$B_\theta = -\partial_r a \, . \tag{$II.6$}$$

The boundary conditions are partially Dirichlet (across the inlet, and based on the mean energy flux) and partially Neumann over the conducting surfaces, also shown in Fig II.1 . The extinction of the axial electric field on the axial conducting boundaries in the feed domain requires that $\phi(z) = \phi_{inlet} - \int dz \frac{1}{c}\partial_t A_z$ but the implied axial variation in ϕ is small. A second drawing (Fig. II.2) shows the scalar potential solution with the gas domain and power feed domains indicated; a third (Fig. II.3), the electric field magnitudes for axial and radial components arising from the scalar potential only. Note that, for the relatively low frequencies characteristic of the Phoenix prepulse, it is only the very small axial field component in the power feed domain that must be balanced by the vector potential component $\frac{\omega}{c}a$ in order to extinguish the tangential field on the conductor surfaces.

As the frequency is increased into the microwave domain the coupling from the vector potential to the scalar potential boundary condition becomes stronger but the coupling back from the scalar

Fig II.2

Phoenix Scalar Potential Solution

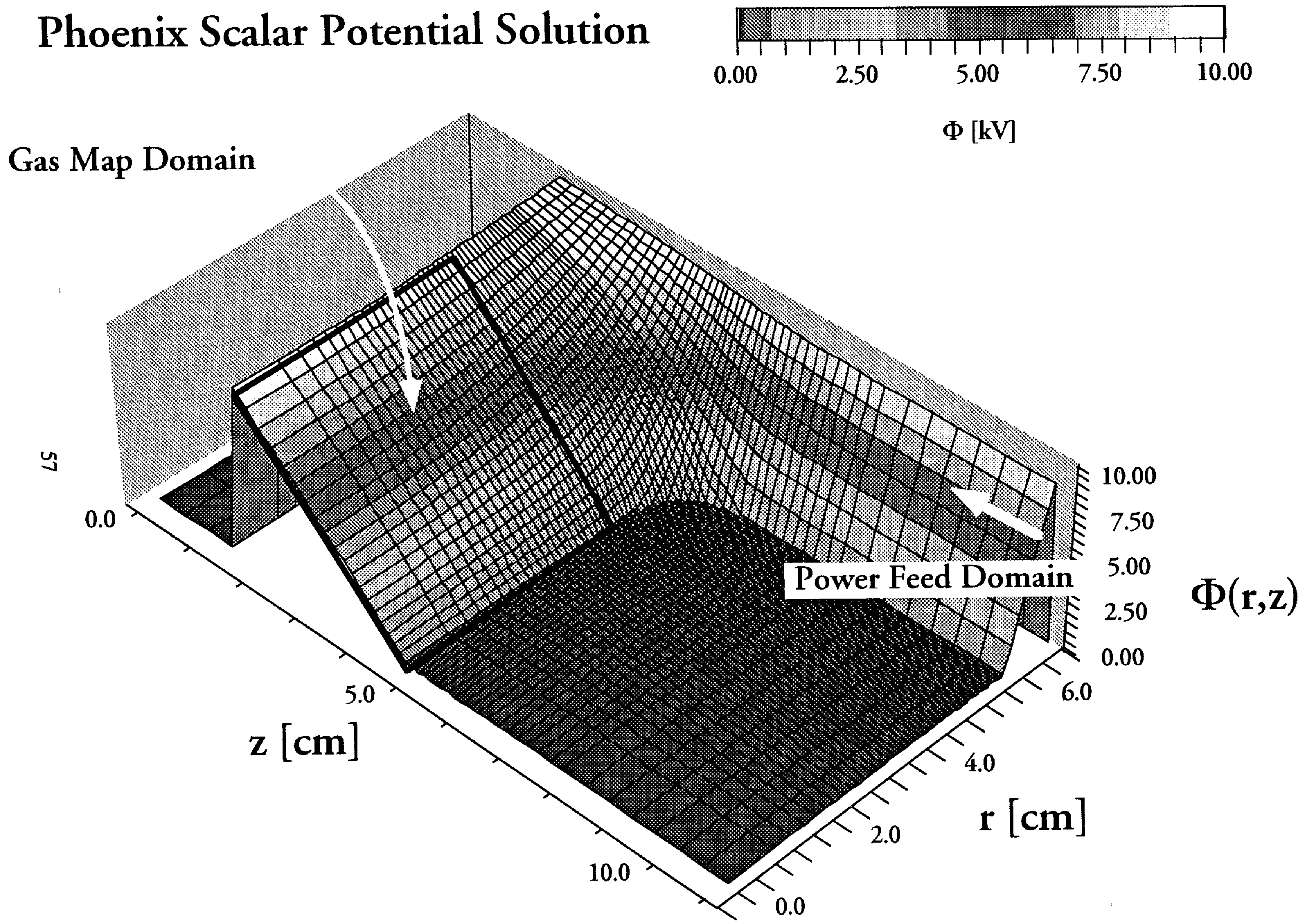

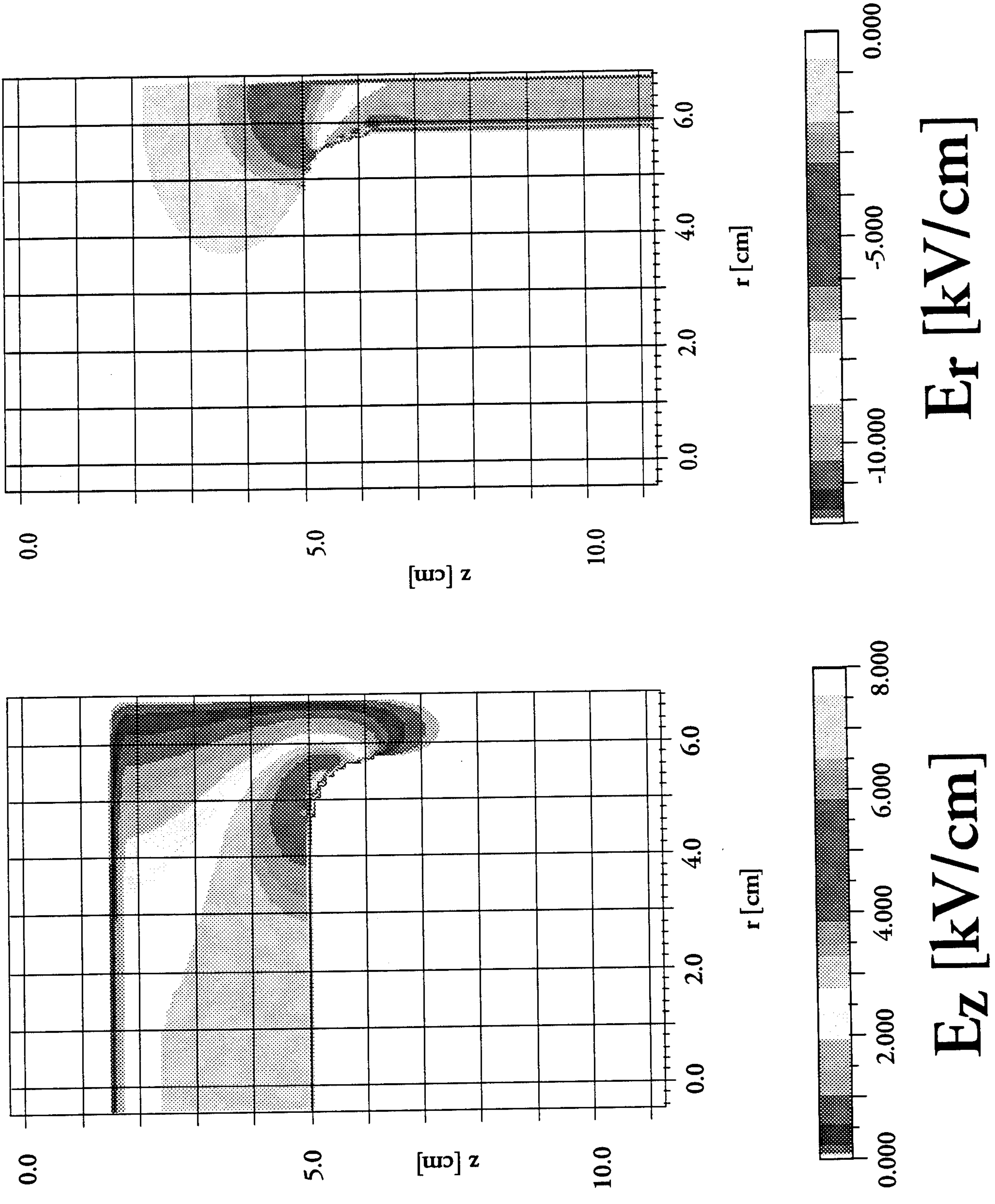

z [cm]
0.0
5.0
10.0
r [cm]
0.0
2.0
4.0
6.0
0.000
-5.000
-10.000
E_r [kV/cm]
z [cm]
0.0
5.0
10.0
r [cm]
0.0
2.0
4.0
6.0
0.000
2.000
4.000
6.000
8.000
E_z [kV/cm]

Fig II.3

potential to the source term in the vector potential problem never turns on unless there is bulk conduction in the gas domain.

Ionization Model

For the purposes of obtaining the initial conditions for puff gas plasma loads, the first level of approximation is clearly to neglect bulk conduction and seek to establish the most likely breakdown paths in the gas load domain. The first requirement for this process is to calculate the expected prepulse for the Phoenix line. Application of the full transmission line model using a variable impedance load element results in the behavior shown in Fig. II.4. Here an implied voltage in the vicinity of the load cavity as large as 25 kV is shown during a model breakdown event at a preset time. The energy available to the neutral gas can vary between 0.15 and 100 J depending upon the precise impedance history for the load.

In the limit of this kind of very fast ionization, which essentially freezes the load gas in place, the change in the electric field pattern as the conductivity rises will not tend to change the breakdown location, although it will certainly be the primary factor in determining the net energy input, which is sensitive to the impedance history. This stroboscopic assumption is justified because the final ionization rates obtained, from both the simple and the detailed models discussed below, show an extreme dynamic range over the spatial domain, implying breakdown times under 10 ns in the most favorable regions.

Argon is well known as an easy gas to break down[5], a fact that might seem at variance with its relatively high ionization potential of 15.76 eV. The paradox is resolved by noticing the very rapid decay of the momentum transfer cross-section with increasing speed[6], which allows free electrons to attain rather high energies in a system like the Phoenix gas puff. As will become apparent below, the lower density areas of the puff allow a free electron to drift at essentially its free fall speed in the applied field, viz. the drift energies will easily approach 15 keV. The ionization process must then proceed from a wide domain of electron energies.

For the development to follow a standard scale field strength E_{sc} of 3 kV/cm (or 10 stV/cm for cgs formulations) and scale neutral density n_{sc} of $1.0 \cdot 10^{17}$ cm^{-3} are used to normalize the

Fig II.4

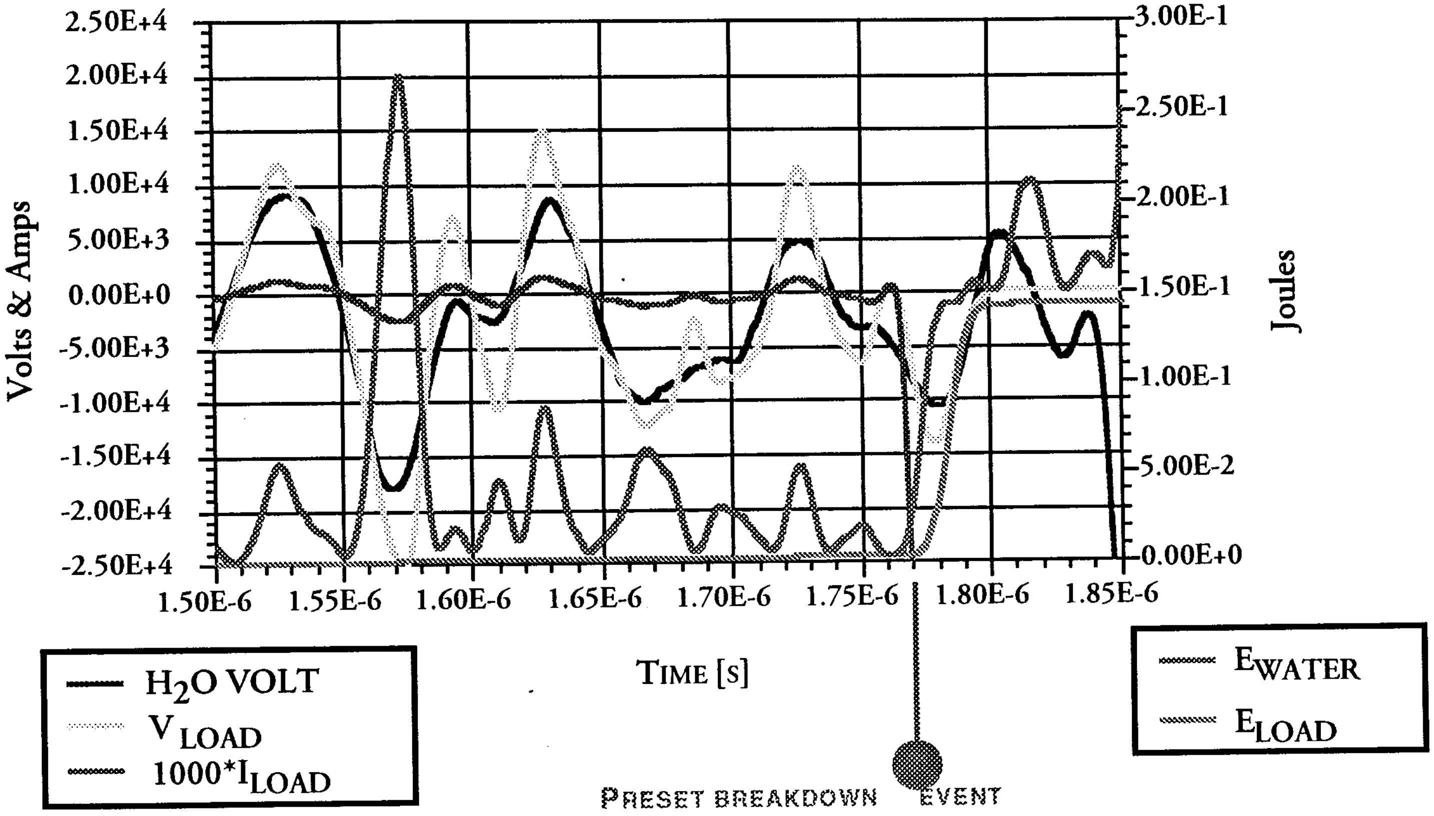

Prepulse detail in a variable model gas load (16 nh , 10 kΩ) —

- 0.15 J energy transfer for short (5 ns) breakdown time, but longer breakdown times transfer up to 100 J
- 15 kV "RF-like" early drive at low current
- only about 0.25 J is available downstream

problem. All cross sections are expressed as functions of energy in eV and normalized to unity, i.e. $\tilde{\sigma}(\mathcal{E}) \leq 1$. All frequencies are normalized to 10 MHz.

Because in the denser regions of the load gas the collision frequency ν_m is much larger than the RF like prepulse frequency, a reasonable estimate of the electron drift energy is furnished by the terminal velocity constraint:

$$m_e \nu_m v_D = eE_{eff} \,, \tag{II.7}$$

where $\nu_m = n v_D \sigma_m(\mathcal{E})$ and the effective field $E_{eff} = E_p/\sqrt{2} \cdot \sqrt{1 + (\omega/\nu_m)^2)}$. Clearly the effective electric field itself depends on the collision frequency and the drift energy, and this dependence can be formulated as

$$\mathcal{F}(\mathcal{E}) \equiv \sqrt{1 + (\omega/\nu_m)^2)} = \sqrt{1 + \frac{5.34 \cdot 10^{-5}}{\mathcal{E}} [\frac{\omega n_{sc}}{\omega_o n} \frac{1}{\tilde{\sigma}_m(\mathcal{E})}]^2} \,. \tag{II.8}$$

Recast as a constraint on the drift energy, the terminal velocity relation becomes

$$\mathcal{E} = \frac{7.31}{\tilde{\sigma}_m(\mathcal{E})\mathcal{F}(\mathcal{E})} [\frac{E}{E_{sc}} \frac{n_{sc}}{n}] \; [eV], \tag{II.9}$$

and can be solved for the terminal drift energy, $\mathcal{E}_D$. As stated above, in many regions of the Phoenix puff, this terminal speed constraint has no solution, any free electrons initially runaway to a freefall speed,viz. $\mathcal{E}_D = e\Phi(r,z)$.

Expected Patterns of Breakdown

Once a solution for $\mathcal{E}_D(r,z)$ is found one may estimate the number of ionizations in a given volume of gas as a product of the ionization rate[7] at $\mathcal{E}_D(r,z)$

$$\nu_i = (\frac{n}{n_{sc}}) \sqrt{\mathcal{E}_D} \tilde{\sigma}_i(\mathcal{E}_D) 1.69 \cdot 10^9 \; s^{-1} \tag{II.10}$$

and the electron transit time in an active region. Here the characteristic length of an active region can be set by the experimental resolution to about 0.5 cm, so the number $\mathcal{N}$ of ion pairs formed in a transit time is

$$\mathcal{N} = 28.5(\frac{n}{n_{sc}}) \tilde{\sigma}_i(\mathcal{E}_D) \,. \tag{II.11}$$

A mapping of the implied ionization zones is shown in Fig. II.5. These model results are encouraging but also point out the need for several obvious improvements to this simple model. First, the pattern does not actually connect a circuit, for this some allowance for diffusion and electron transport must be added. Second, the dynamic range of ionization is too large, indicating that a full ionization balance must be computed and allowed to feed back on the electric field strength and attenuate it throughout the ionization timeframe using a calculation of the self-consistent conductivity. Finally, the distribution function will not be that of a drifting beam in most relevant parts of the real diode, but a non-Maxwellian form dependent on the scattering from excited states and on the time dependent excited state populations.

As a means of checking the ionization predictions from the simple model above, the Boltzmann equation was solved for a simplified Ar model employing only the ground state and four excited states. Included as well were ionization, recombination, and momentum transfer to the neutrals. The solver has been tested on simple cases and modified to show the time history of the evolving distribution function. The advantages to this more detailed effort are primarily that the conductivity and the time dependence of the ionization can be examined in the expected E/N domains that are implied by the measured N values and the computed E values. At the location of the large ionization rate shown above (Fig. II.5) near z= 1.0 cm and r=1.5 cm, the distribution function would first be Druyvesteyn in the core and Maxwellian above about 30 eV for perhaps 60 ns or so as the field strength builds to about 20% of its peak value. However, once the field reaches twice that value, the ionization to 2% would proceed in about 6 ns and strongly modify any future increase in electric field at that point. The final distribution function for the discharge will closely approach a Maxwellian as the conductivity rises, c.f. Fig II.6.

The Boltzmann solution therefore supports the central inference from the simple model — the conductivity tends to peak where the density is falling rapidly to the exterior against a more slowly varying electric field strength. The "bad news" is that the conductivity is clearly strong enough to modify the field profile significantly.

Fig II.5 Expected breakdown sites from the simple model

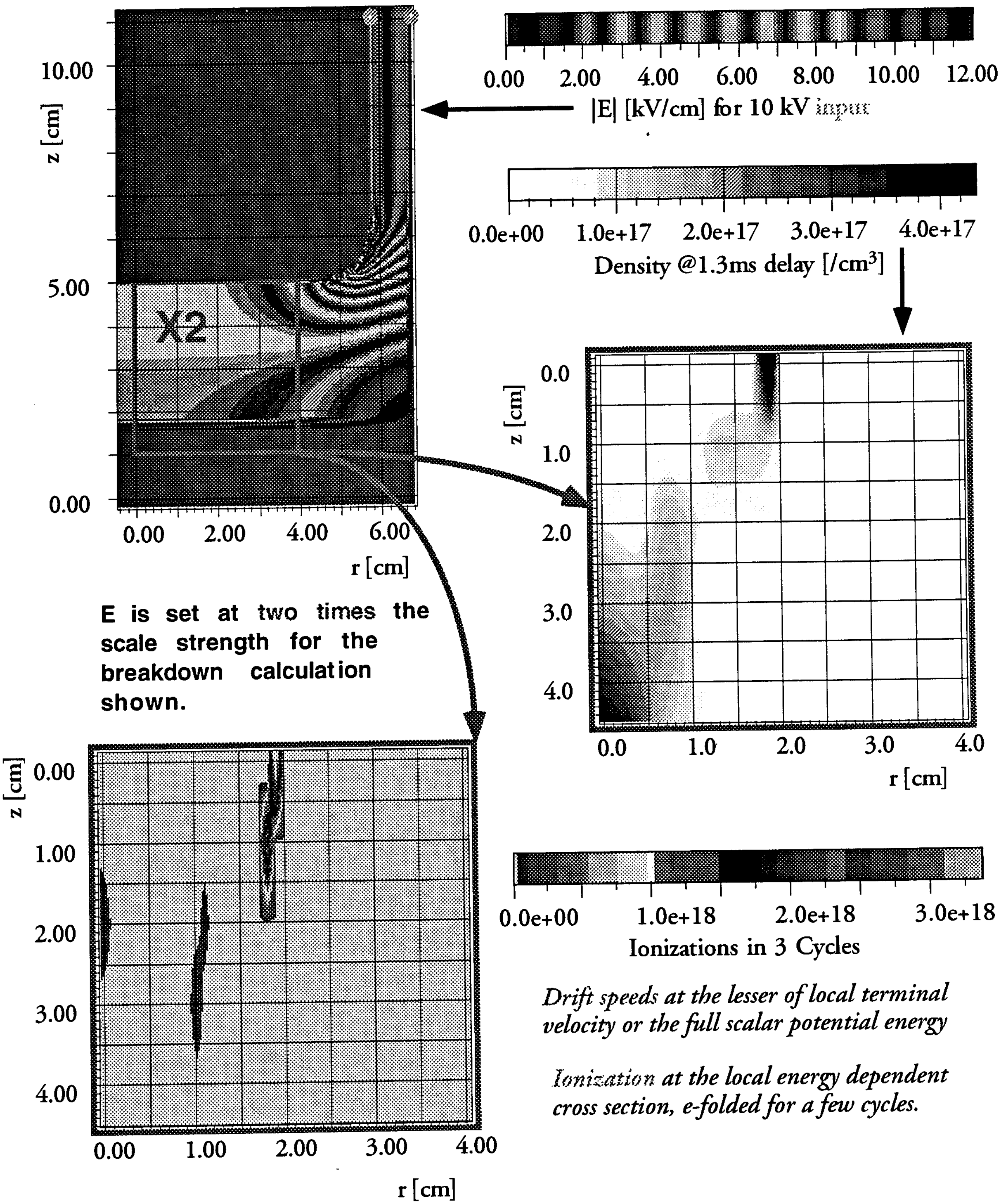

E is set at two times the scale strength for the breakdown calculation shown.

Drift speeds at the lesser of local terminal velocity or the full scalar potential energy

Ionization at the local energy dependent cross section, e-folded for a few cycles.

Fig. II.6 Boltzmann Ar Solution and
CALCULATED ELECTRON TRANSPORT COEFFICIENTS

Drift Velocity (cm/sec)	Drift Energy (eV)	Characteristic Energy (eV)	Conductivity (1/sec)
7.940E+07	1.792E+00	1.151E+01	1.968E+13

ELECTRIC FIELD PARAMETERS

E/N (V-sq.cm)	E/P (V/cm/Torr)
1.135E-14	3.654E+02

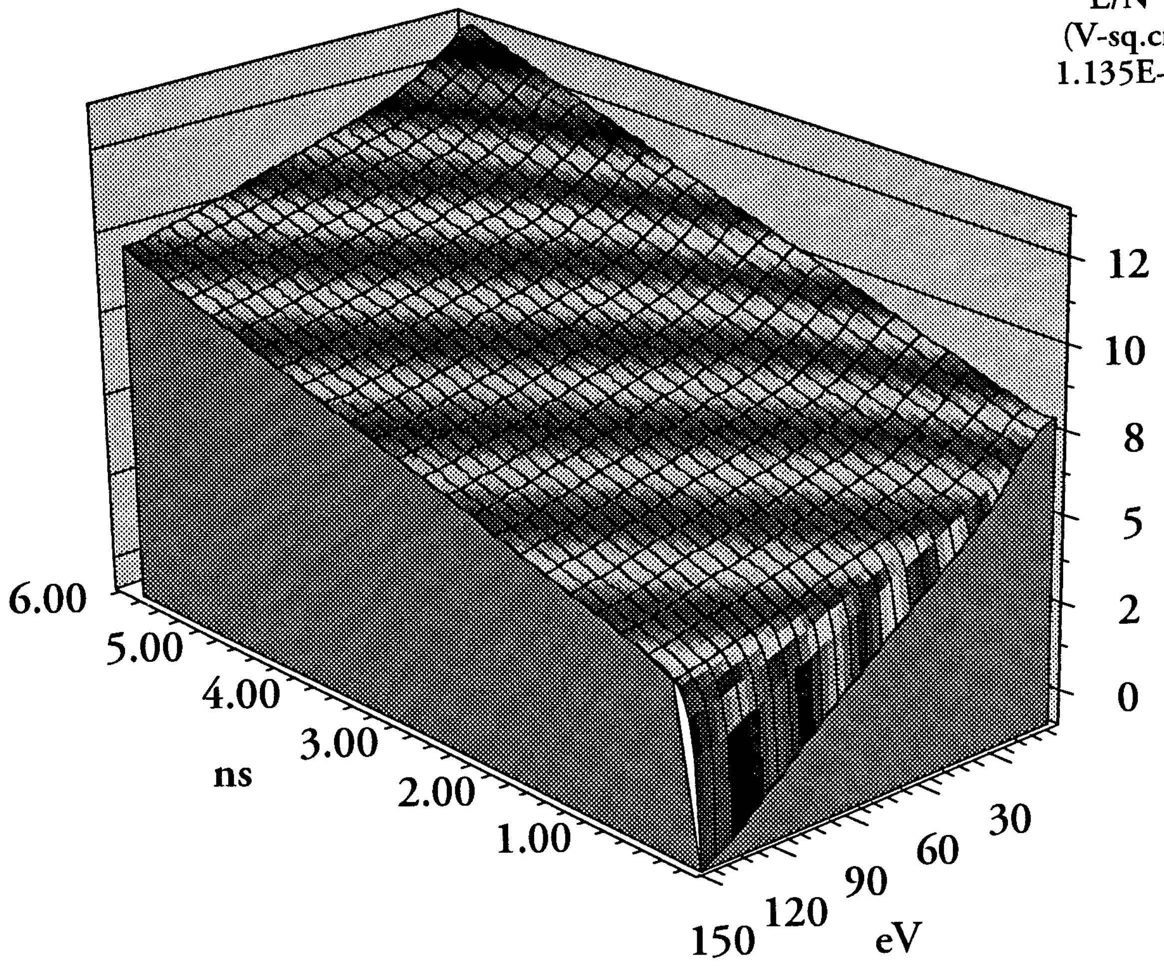

III. ARGON GAS PUFF IMPLOSION PERFORMANCE (1D MHD)

Methodology

In this section are summarized the results from numerical simulations of argon puff gas loads on the original Phoenix x-ray simulator before the new insulator stacks were deployed. The investigation focused on providing argon K-shell yield predictions and load performance for a variety of initial conditions. The numerical simulations were carried out using two methods: first, a scaling law model adjusted for low $\eta^\star$-values (where $\eta^\star$ is the ratio of kinetic energy to the sum of the internal and thermal energies required to get into the K-shell) and secondly, a 1-D multi-zone non-LTE radiation hydrodynamics model, DZAPP[8] self-consistently coupled to a driving circuit representative of the Phoenix generator. The scaling law calculations provide a ballpark estimate of the K-shell yield for given external load conditions such as mass, radius, and length. This approach provides a roadmap localizing the parameter space for detailed simulations. The second series of calculations was carried out using a two temperature DZAPP radiation MHD model which includes a multi-level collisional radiative equilibrium description of the ionization physics and has an extensive L- and K- shell level structure. The total radiative yield includes contributions from bremsstrahlung, recombination radiation, and line radiation. Opacity and radiation transfer are also accounted for in DZAPP. The voltage waveform driving the circuit was representative of the Phoenix generator and produced a self-consistent current profile. For the initial series of simulations the length of the puff was chosen as 2 cm. The calculations were performed for a thin shell with a nonuniform density profile and a uniform fill density profile, that is actually more representative of longer gas puff distributions. Finally, calculations were performed for load lengths of 3 and 4 cm in order to compare with the 2 cm runs as well as recent experimental results and to asses the influence of load length on the K-shell performance of Phoenix.

Scaling Law Formulation and Results

The K-shell yield per unit length, kJ / cm, can be written as

$(Y_K/\ell) =$ smaller of

$$10^6 \epsilon_L(\eta^\star)(\frac{0.5}{R_f})a_0(\eta^\star)a_Z(Z)(\frac{M}{\ell})^2, \qquad (III.1a)$$

$$10^{-1}\epsilon_L(\eta^\star)\epsilon_K(v^2/2)(\frac{M}{\ell}), \qquad (III.1b)$$

where M is the total mass loading in mg, ℓ is the pinch length in cm, R_f is the final implosion or stagnation radius where the plasma reaches the implosion velocity, v in cm / μs. The parameter $\eta^\star$ is defined through the relation $\eta^\star = (m_i v^2/2E_{min})$, where v is the final maximum implosion velocity and E_{min} is the minimum energy needed to reach and maintain an individual atom in the K-shell. From the scaling laws of ref. [9] the following simple relationships were determined: $m_i \approx 1.6Z^{1.1}m_p$ and $E_{min} \approx 1.5Z^{3.5}$ eV / ion. Here m_p is the proton mass and E_{min} is the minimum energy required to strip and maintain the atom with an abundance of 50% hydrogenlike and 50% heliumlike ionization stages.

The coefficients can be written as

$$a_0(\eta^\star) = 33.7 + \frac{595}{\eta^\star} - \frac{70.7}{\eta^{\star 2}}[kJcm/mg^2]),$$

$$a_Z(Z) = \frac{exp(-20.6/Z^{0.9})}{Z^{3.55}},$$

$$\epsilon_K = 0.3 \qquad (III.2)$$

The function $a_0(\eta^\star)$ is based on 1-D multi zone numerical simulations for high $\eta^\star$ implosions with aluminum. These radiation MHD simulations employ a linear rising current ramp until the outer radius of the plasma reaches 0.14 cm, after which the current is turned off in order that the K-shell yield reflect only the kinetic energy input. The current cutoff radius is larger than the final compression radius of the pinch. ϵ_K is also determined from these simulations and represents the conversion efficiency of total kinetic energy into K-shell radiation. The actual calculations display a range for ϵ_K from 0.25 to 0.5, but for the present discussion it is fixed at a conservative value of 0.3. The expression for $a_Z(Z)$ is based upon Z-scaling of the He_α line radiation in the coronal approximation.

The two remaining factors in Eqs. (1) and (2), R_f and ϵ_L ($\eta^\star$), arise from revisions adjusting the data to agree with experiment. The form of the R_f dependence in eq. (1) derives from the expression for optically thin line emission. The second factor $\epsilon_L(\eta^\star)$, concerns a reduction of the K- shell yield for implosions with η near unity. Clearly, there is no K-shell yield for $\eta^\star$ = 0, while

$\eta^\star \gg 1$ should smoothly join the relations given by eqs. (1) and (2). For simplicity it is assumed that ϵ_L varies linearly with $\eta^\star$ in the vicinity $\eta^\star$ 1. Based on a number of numerical simulations the resultant form for the low $\eta^\star$ correction of eqs. (1) and (2) is given by

$$\begin{array}{c} 1\;,for\;\eta^\star \geq 3; \\ \epsilon_L(\eta^\star) = 0.2(2\eta^\star - 1)\;,for\;0.5 \leq \eta^\star \leq 3; \\ 0\;,for\;\eta^\star\; \leq 0.5\;. \end{array} \qquad (III.3)$$

The complete K-shell radiation scaling law can be written functionally as

$$Y_K = Y_K(Z, R_f, \ell, v_{imp}, M)\;. \qquad (III.4)$$

For a chosen load material (Z) and final radius (R_f), the K-shell yield (Y_K) per unit length (ℓ) can be calculated as a function of the implosion velocity (v) and mass loading (M) per unit length. The yield thus depends solely upon the plasma conditions at implosion.

Figure III.1 presents contours of the argon K-shell yield in kJ as a function of load mass and initial radius for a 2 cm long gas puff. The table on the right side of the Figure represents K-shell yields; the outer contour on Fig.1 corresponds to the last value listed in the yield column. **Reading inward on the contour plots corresponds to reading upward in the table.** The outermost contour corresponds to the last entry in the table under K-shell yields and has a values of 0.10 kJ. The innermost contour corresponds to a value of 7 kJ. The "H" located in the innermost contour and listed as ZHGH corresponds to the highest yield value which in this case is 9.59 kJ and has a mass (XHGH) of 0.265 gm and a radius (YHGH) of 1.62 cm. The contours of constant K-shell yield extend over a broad range of initial radii and mass. However, for the optimum yield the contour converges on a smaller restricted region surrounding the "H" as seen on the Figure.

MHD Simulations

The numerical simulations presented here to characterize the dynamics of a radially imploding Z-pinch plasma are based on a one-dimensional two temperature multi-zone non-LTE- radiation-

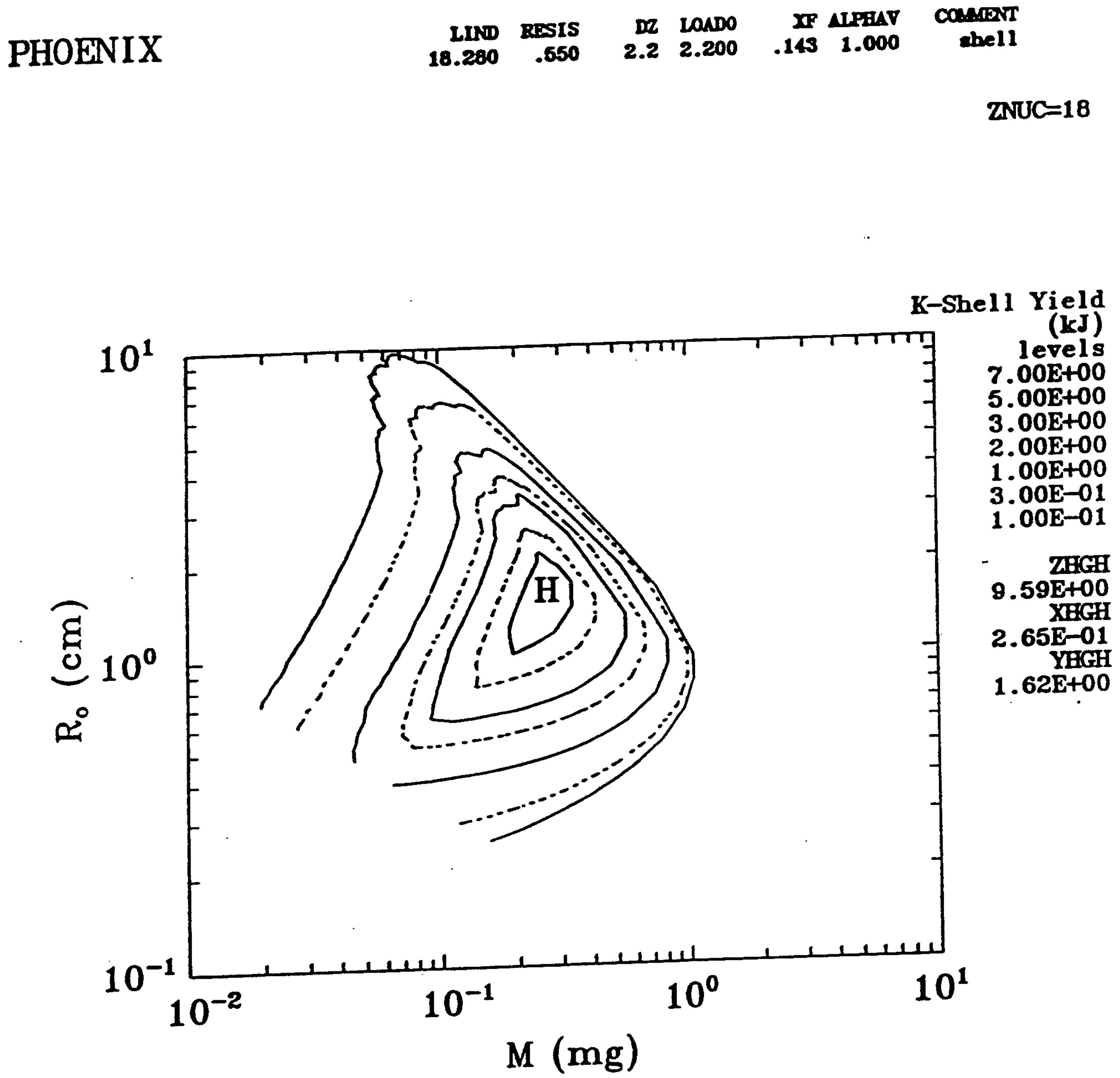
PHOENIX
LIND 18.280
RESIS .550
DZ 2.2
LOADO 2.200
XF .143
ALPHAV 1.000
COMMENT shell
ZNUC=18
K-Shell Yield (kJ) levels
7.00E+00
5.00E+00
3.00E+00
2.00E+00
1.00E+00
3.00E-01
1.00E-01
ZHGH
9.59E+00
XHGH
2.65E-01
YHGH
1.62E+00
H
10^1
10^0
10^{-1}
R_o (cm)
10^{-2}
10^{-1}
10^0
10^1
M (mg)

Fig. III.1

magnetohydrodynamic model, DZAPP, with a transmission line circuit model for the driving generator. In a cylindrical coordinate system (r,z,t) the standard equations of continuity,

$$\frac{\partial}{\partial t}(\rho) + \frac{1}{r}\frac{\partial}{\partial r}(r\,\rho u) = 0 \qquad (III.5),$$

total momentum,

$$\frac{\partial}{\partial t}(\rho\, u) + \frac{1}{r}\frac{\partial}{\partial r}(r\,\rho\, u^2) + \frac{\partial(\,p_i + p_e)}{\partial r} + \frac{1}{r}\frac{\partial}{\partial r}(r\, Q_{vis}) = -\frac{1}{c}J_z\, B_\phi \qquad (III.6),$$

and ion internal energy,

$$\frac{\partial}{\partial t}(\rho\,\varepsilon_i) + \frac{1}{r}\frac{\partial}{\partial r}(r\,\rho\,\varepsilon_i\, u) + p_i\frac{1}{r}\frac{\partial}{\partial r}(r\, u) - \frac{1}{r}\frac{\partial}{\partial r}(r\,\kappa_i\frac{\partial T_i}{\partial r}) + Q_{vis}\frac{\partial u}{\partial r} = Q_{ie} \quad (III.7a),$$

and electron internal energy,

$$\frac{\partial}{\partial t}(\rho\,\varepsilon_e) + \frac{1}{r}\frac{\partial}{\partial r}(r\,\rho\,\varepsilon_e\, u) + p_e\frac{1}{r}\frac{\partial}{\partial r}(r\, u) - \frac{1}{r}\frac{\partial}{\partial r}(r\,\kappa_e\frac{\partial T_e}{\partial r}) =$$

$$-\,Q_{ie}\frac{\partial u}{\partial r} + \eta\, J_z^2 - \Lambda \qquad (III.7b),$$

are integrated over each radial zone and then followed in a Lagrangian fashion. Here ρ is the mass density, u the mass weighted radial velocity, p_i the ion pressure, p_e the electron pressure, Q_{vis} the rr component of a tensor artificial viscosity for smoothing shocks, J_z the axial current density in the pinch, B_θ the azimuthal magnetic field, ε_i the specific internal energy per unit mass of the ions, ε_e for the electrons, T_e the electron temperature, T_i the ion temperature, κ_e the electron thermal conductivity, κ_I the ion thermal conductivity, η the electrical resistivity, and Λ the radiation cooling (negative) or heating (positive) rate. The transport coefficients $\kappa_{e,i}$, η , and the ion-electron equilibration rate $Q_{e,i}$ are taken from Braginskii.[10] The numerical or artificial viscosity Q_{vis} for Lagrangian type codes is fully discussed by Schulz.[11] In the present paper we use $Q_{vis} = \beta\rho\Delta u C_s$, where Δu is the velocity difference across a zone and C_s is that zone's sound speed. Q_{vis} is zero if the zone is expanding. A large β parameter value of 10 is used to soften the Z-pinch implosion and prevent radiative collapse. Such a viscous enhancement is found to improve the agreement between experiment and simulation for the observed stagnation densities and radii. Admittedly, the large viscous term is used to mimic the effect of presently unknown pinch physics leading to a softened implosion. The current density and magnetic field are related through Ampere's law

$$J_z = \frac{c}{4\pi}\frac{1}{r}\frac{\partial}{\partial r}(r\, B_\theta) \qquad (III.8)$$

.

The magnetic field is determined by an induction equation by combining a generalized Ohm's law with Faraday's law:

$$\frac{\partial B_\theta}{\partial t} + \frac{\partial}{\partial r}(u\, B_\phi) = \frac{\partial}{\partial r}(c\,\eta\, J_z). \qquad (III.9)$$

The ion internal energy includes the ion thermal energy as well as the atomic excitation + ionization specific energy (ε_x):

$$\varepsilon_i = \frac{3}{2}\frac{k_B T_i}{m_i} + \varepsilon_x \qquad (III.10)$$

The electron internal energy is represented by

$$\varepsilon_e = \frac{3}{2} < Z > \frac{k_B T_e}{m_i} + \varepsilon_x \qquad (III.11)$$

where n_i is the ion number density, m_i is the ion mass, k_B is Boltzmann's constant and $< Z >$ is the mean charge per ion.

The transmission line circuit model is similar to the BERTHA code of Hinshelwood.[12]The model follows the forward and backward propagating voltage waves assuming only transverse electromagnetic modes are present. Circuit elements have associated transit times Δt such that a line element of impedance Z has an inductance Z Δt and a capacitance Δt / Z. Wave propagation across junctions between line elements is solved through reflection and transmission coefficients derived from Kirchoff's laws. The junction at the dynamic load is treated implicitly to ensure strict conservation of electrical + plasma energy.

The ionization dynamics and radiation transport are time split from the magnetohydrodynamics, i.e. ε_x and charge state Z are held constant during a hydro timestep. When the excitation (ionization) dynamics is updated within a zone, subject to the conservation of internal energy in that zone, the atomic level populations are determined by a set of rate equations

$$\frac{\partial f_{li}}{\partial t} = \sum_{m} (R_{mli}\, f_{mi} - R_{lmi}\, f_{li}), \qquad (III.12)$$

where f_{li} is the fractional population of level l in the ith ionic species, and R_{lmi} is the net rate describing the transition in the ith species from the initial level m to the final level l. The net rate includes collisional ionization, excitation, de-excitation, 3-body and radiative recombination, photoionization, pumping and radiative decay.

Radiation emission, including opacity effects, from the plasma are dependent upon the local atomic-level populations, for not only are photons created by radiative recombination and decay, such photons also lead to population redistribution. Thus the ionization dynamics and radiation transport are a strongly coupled interactive problem and must be solved together as demonstrated in ref. 6. The radiation transport of the bound-bound and bound-free transitions are carried out using the probability of escape formalism. Multifrequency transport is performed for the free-free radiation.

Results

For the plasma shell simulations a typical initial mass density profile is shown on Fig. III.2. In this case the total mass is 0.375 mgm, the outer radius is 2 cm, and the length of the puff is 2 cm. Several simulations were performed for the shell configuration and are superimposed on the contour plot. The 1-D MHD K-shell yields are shown as • on Fig. III.3. Similarly, for loads initially configured as uniform fills the K-shell yields are superimposed on Fig. III.4 and identified as •. These results show that the scaling laws provide ballpark estimates for the K-shell yield that are within an order of magnitude from those obtained with a more sophisticated MHD simulation. Actually, in some cases the comparisons are fairly good and within factors of 2 to 3 of each other. Another result of considerable interest is that the uniform fill or constant density simulations are very competitive with the shell simulations for the parameter space investigated. Also, the uniform plasma simulations may better mimic the experimental results since by the time the current peaks the initial plasma shell may begin to look more like a uniform fill. One advantage of uniform fills is that they remain stable to the Rayleigh-Taylor modes for larger diameter loads.

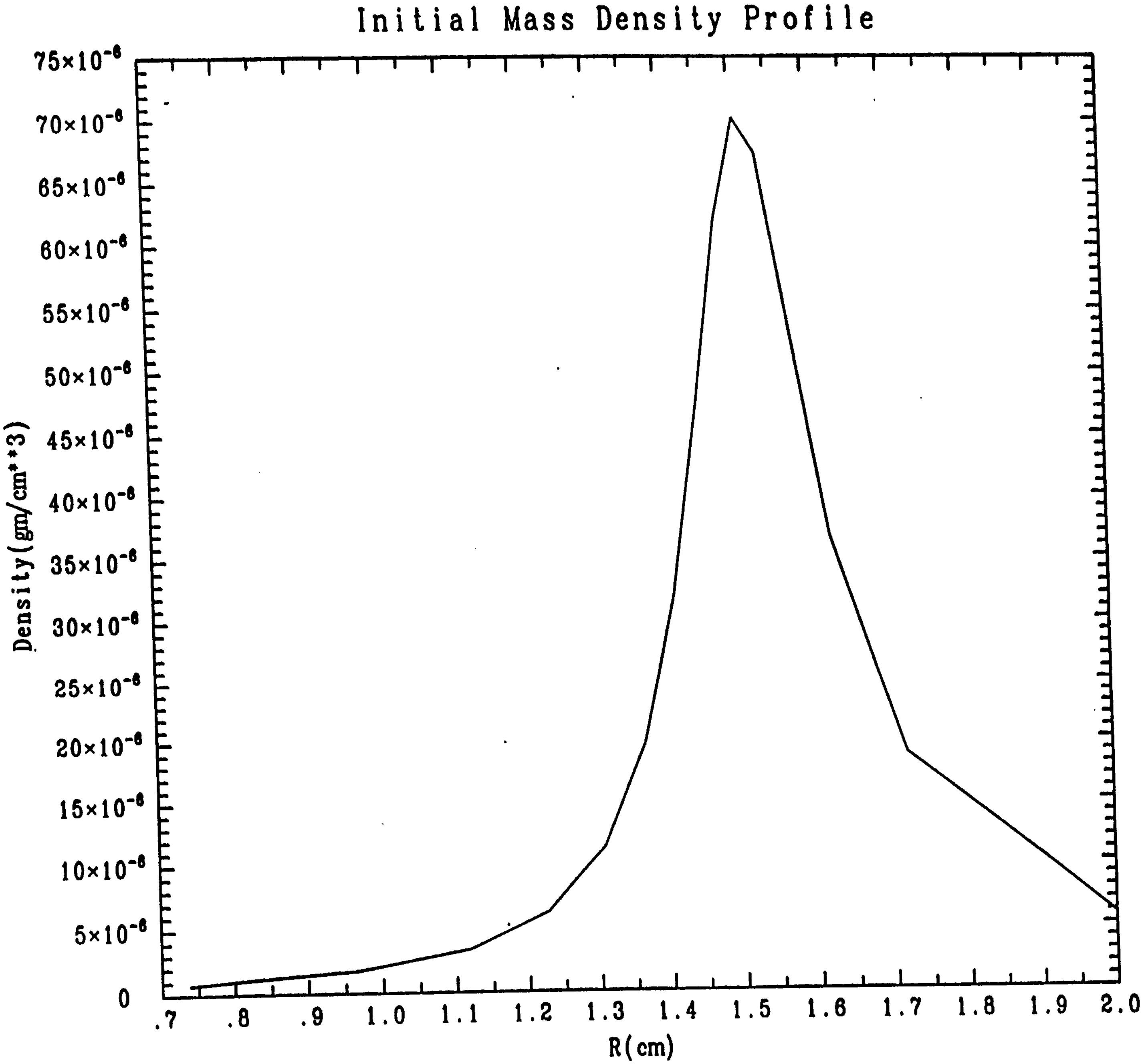

Initial Mass Density Profile

NCELL=15 R0= 2.00 MASS=3.75E-04 DRDEN= 0.20 RCDEN= 1.50 DRGRID=1.65 DZ= 2.0

Fig. III.2

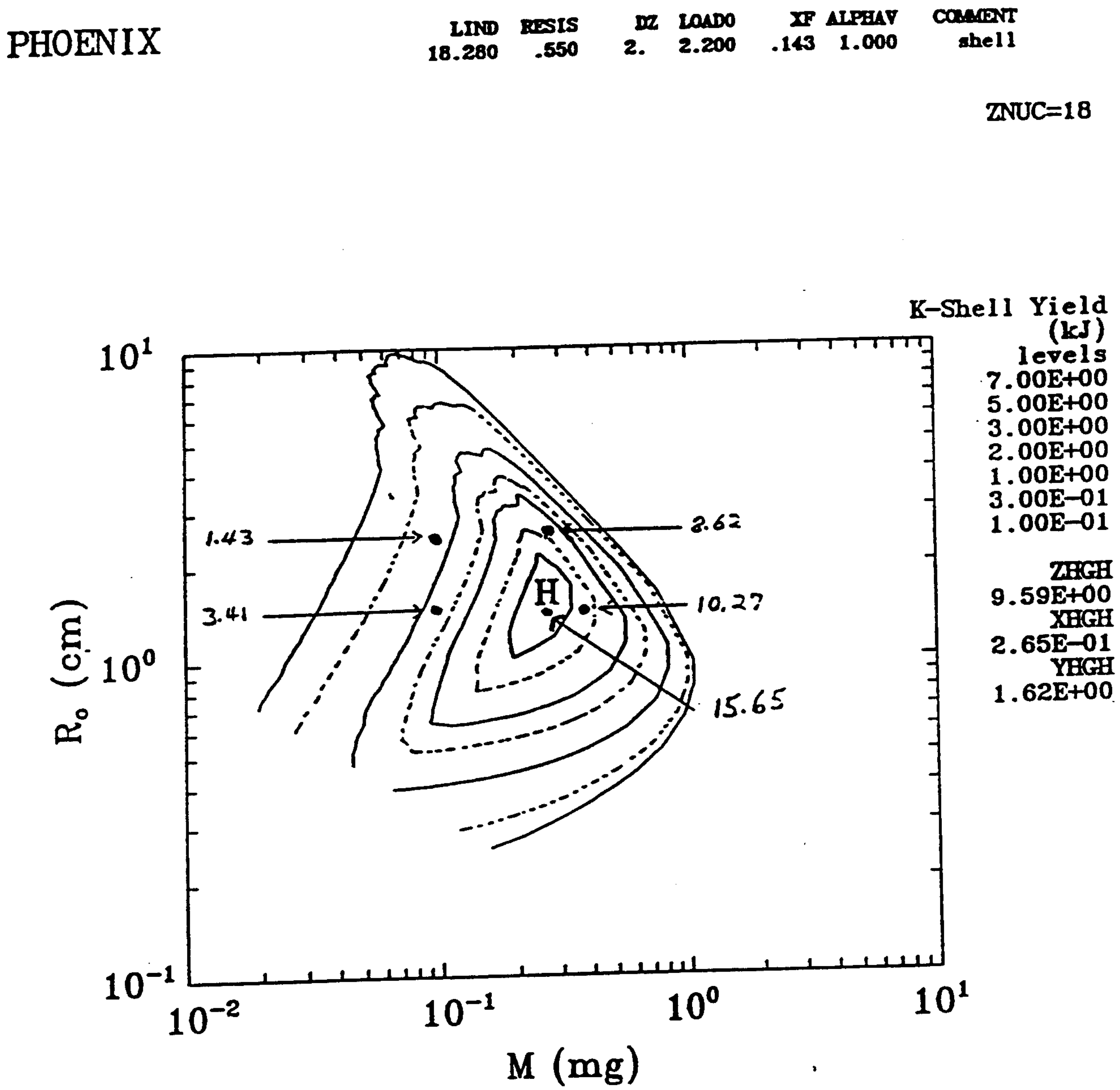

CRE: non-uniform initial ρ(r) profile
Fig. III.3

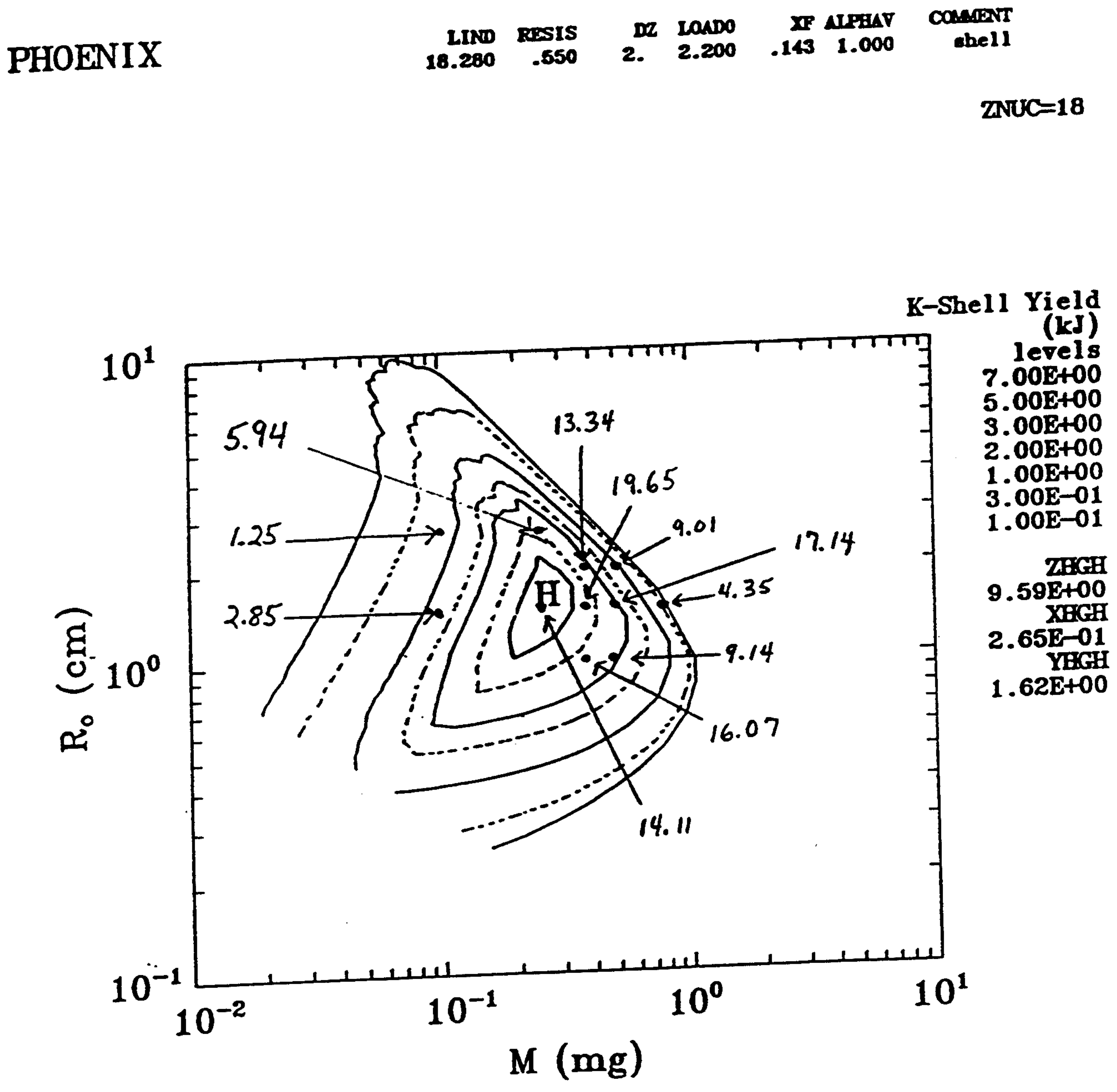

Fig. III.4
CRE: constant initial ρ (r)

A number of additional simulations were carried out for a variety of conditions. These are presented below in the following Tables. The nomenclature used in the Tables is: Y_T represents the total radiative yield, Y_K represents the radiative yield above the K-edge and includes contributions from lines and continuum. For the conditions considered in these simulations the major contribution to Y_K comes from the lines.

ARGON results for Collisional Radiative Equilibrium (CRE): R_0=2.00 cm, l=2.0 cm. For Uniform Fill (UF) R_c=1.0 cm and for Shell R_c=1.50 cm, where R_c is the radius at the center of the mass distribution

Table III.1 ARGON results for Collisional Radiative Equilibrium

MASS [mgm]	*CONFIG* –	Y_T [kJ]	Y_K [kJ]	$\eta^\star$ –
0.25	UF	34.56	9.56	0.807
0.250	Shell	42.19	15.76	1.248
0.375	UF	48.27	12.92	0.592
0.375	Shell	53.09	10.72	0.777
0.500	UF	48.98	8.58	0.432
0.500	Shell	52.64	7.69	0.521
0.625	UF	43.58	2.32	0.312
0.625	Shell	42.38	4.89	0.353
0.750	UF	32.65	0.0012	0.231
0.750	Shell	33.49	2.67	0.247

ARGON results for Collisional Radiative Equilibrium (CRE): R_0=2.00 cm, l=2.0 cm. R_c is the radius at the center of the mass distribution

Table III.2 ARGON results for Collisional Radiative Equilibrium

MASS [mgm]	*CONFIG* –	R_0 [cm]	R_c [cm]	Y_T [kJ]	Y_L [kJ]	Y_K [kJ]
0.10	UF	2.0	0.75	5.69	2.84	2.85
0.10	Shell	–	1.0	6.65	3.24	3.41
0.10	UF	2.5	1.25	2.70	1.45	1.25
0.10	Shell	–	1.50	2.89	1.46	1.43
0.25	UF	2.5	1.25	28.52	22.58	5.94
0.25	Shell	–	1.50	31.53	22.91	8.62

ARGON Shell Collisional Radiative Time Dependent Results for 0.75 mgm, R_0=2.0 cm and R_c=1.5 cm.

Table III.3 ARGON Collisional Radiative, Time Dependent Results

ℓ [cm]	M/ℓ [mgm/cm]	Y_T [kJ]	Y_T/ℓ [kJ/cm]	Y_K [kJ]	Y_K/ℓ [kJ/cm]	$\eta^\star$ –
2.0	0.375	34.25	17.12	0.252	0.126	0.204
3.0	0.250	70.97	23.66	4.92	1.64	0.387
4.0	0.1875	96.70	24.18	10.20	2.55	0.537

ARGON Collisional Radiative Time Dependent Results for a Uniform Fill with 0.375 mgm, R_0=1.5 cm.

Table III.4 ARGON Collisional Radiative, Time Dependent Results

ℓ [cm]	M/ℓ [mgm/cm]	Y_T [kJ]	Y_T/ℓ [kJ/cm]	Y_K [kJ]	Y_K/ℓ [kJ/cm]	$\eta^\star$ –
2.0	187.5	62.9	31.45	17.8	8.90	0.550
3.0	125.0	55.7	18.57	17.62	5.87	0.617
4.0	93.75	50.2	12.55	14.01	3.50	0.652

ARGON Collisional Radiative Time Dependent Results for a Shell with 0.375 mgm, R_0=2.0 cm, R_c=1.5 cm.

Table III.5 ARGON Collisional Radiative, Time Dependent Results

ℓ [cm]	M/ℓ [mgm/cm]	Y_T [kJ]	Y_T/ℓ [kJ/cm]	Y_K [kJ]	Y_K/ℓ [kJ/cm]	$\eta^\star$ –
2.0	187.5	57.5	28.75	9.30	4.65	0.663
3.0	125.0	67.10	22.37	15.98	5.33	0.966
4.0	93.75	59.70	14.92	18.73	4.68	1.143

IV. Conclusions

Power Flow

The voltage and current sensors in the Phoenix line are in need of a general and thorough recalibration. The primary candidates are the voltage monitors associated with the transfer capacitor, first transformer, and perhaps the water monitor. Further work to check and, if necessary obtain, more azimuthal symmetry in current sensors would also be advisable.

The primary load energy loss mechanism in this machine is premature insulator flashover. The characteristics of the flashover have been modeled quite successfully by a variety of shunt elements. The new insulator stacks must be the first recourse in solving this problem. Secondary losses to vacuum electron flow may also be important, but these could be due to lower magnetic insulation when the front end current fails to reach its expected value due to the present insulator performance.

The primary breakdown mechanism for Ar gas loads is the substantial prepulse. The prepulse levels consistent with other verifiable voltages and currents in the line are more than enough to ionize the load. Ionization appears to occur predominantly on the descending slope of the density profiles, indicating that preionization schemes involving electric field profile conditioning must be designed for a particular gas jet firing delay because of the very complex flows and compressions observed in the present nozzle.

The interplay between breakdown sites and mass loading can partially determine the zippering behavior of the PRS loads. Our experience with the MHD code would indicate an ability to change the zipper sequence significantly with small mass profile changes, but more work is needed to establish the proper linkages between the breakdown model and the MHD code.

A continued effort to develop and validate the early time breakdown model used here is important for other DNA activities involving gas puff loads. As more energetic machines come into general use, the ability to control early breakdown to set the load mass in gas is a fair target research. If pursued it may be the best hope for precise yield control.

Yields

There are several conclusions that can be drawn from these results. Scaling laws can provide a sense of magnitude for the yields. Unfortunately, in comparison with detailed calculations significant discrepancies often arise vitiating as well as questioning the validity of scaling laws for anything but order of magnitude estimates. Scaling laws are useful for suggesting trends but they are no substitute for detailed simulations. Also, scaling laws say nothing about the quality of the spectrum of emitted radiation or pulse duration.

For the conditions chosen in Table III.1 for the equilibrium simulations the total yield from both the shell and uniform fills are about the same as is the case for the K-shell yields except for the heaviest mass load where the uniform fill did not get hot enough to significantly populate the K-shell. Similar conclusions hold for the results presented in Table 2 for slightly different radii. Also included in Table III.2 are the L-shell contributions. For lower mass loads the K- and L-shell contributions are about equal indicating that at assembly the plasma is heated into the K-shell. For the highest mass loading in Table III.2 most of the plasma remains in the L-shell for both the uniform fill and the shell. The last three Tables represent the results for both time dependent simulations and differing lengths. From Table III.3 we see that the yield for the shell increases as the length increases from 2 to 4 cm. The trend is the same for the uniform fill but appears to saturate between 3 and 4 cm. in length. A comparison between the entries in Table III.5 with Table III.3 indicates that 0.375 mgm is a better mass loading that the heavier 0.75 mgm for K-shell yields. Also, a comparison between time dependent and equilibrium calculations shows that the K-shell yields predicted from the time dependent calculations are in general less than the corresponding equilibrium values. The comparison between equilibrium and time dependent treatments diverge the higher the Z of the load because of the time it takes to ionize to the L- and K- shells which may limit the yields. Time dependent scaling laws need to be invented to predict estimates for yields from higher-Z loads. All in all, the $\eta^\star$ values are consistently less than unity except for a few simulations indicating poor implosions. When the new insulator stacks are installed in the Phoenix system and the circuit is available a new series of simulations will be initiated to determine loads for optimum yields.

Appendix: 2-D Phoenix simulations with modified resistivity.

Several simulations using a modified resistivity during the initial phase of the implosion were run in order to access the importance of the initial current flow pattern on the pinch dynamics. In particular, if the initial current flow is such that mass is left behind during the runin phase of the implosion, it might be expected that both the peak kinetic energy and radiative output of the load would be smaller. This might account for the relatively lower yields measured in Phoenix experiments as compared to numerical simulations. Argon K-shell yields are in the range 15 - 20 kJ in our two dimensional simulations.

Initial current paths were modeled by imposing a large resistivity to selected regions on the outside of the pinch during the initial phase of the implosion. This allows the magnetic field to penetrate into this region. One consequence is that the magnetic pressure gradient driving the implosion will be reduced. This idea was tested against a standard implosion using numerical output from the NRL density mapped nozzle profile. The standard implosion produced an Argon K-shell yield of 17 kJ. The total yield, K-shell plus the radiative output produced by the limited L-shell model, was 33 kJ. When the resistance on the outside of the pinch was raised during startup, which was defined as the first 50 nsec of the implosion, to allow full penetration of the field (resistive diffusion multiplied by a factor of 10^7 for diffusion purposes but not included in the ohmic heating term) the results were lower by about 1 kJ, i.e. 16 kJ K-shell and 32 kJ total. The implosion time was also decreased by 2 nsec. This indicates that the mass participating in the implosion was reduced However, from a numerical standpoint both changes can be considered to be insignificant.

Unfortunately, the model which was used in our simulations did not provide many differences in the final implosion. A possible reason for the failure of our resistive model is that although there is an early time initialization of the current path, at later times the heating on the outside of the pinch also results in the current moving outside of most of the mass. This allows all, or most, of the mass to be swept up by the field since this process occurs on a time scale shorter than the implosion. The idea that the initial current path may change the dynamics of the implosion may still be able to be validated by numerical simulations if a correct model which establishes and maintains the current profile can be found.

Acknowledgements

This work was supported jointly by DNA/TDSP and NSWC/Phoenix Facility.

References

1. R. E. Terry, F. L. Cochran, NRL/MR/6720-94-7428

2. ibid., p. 5

3. G. Peterson, B. Weber, private communication.

4. J. Creedon, J. Appl. Phys **48**(3), 1073(1977)

5. W. Scharfman, T. Morita, JAP **35**(7), 2016(1966),

6. S. C. Brown *Basic Data of Plasma Physics*, MIT PRESS, 1959, p. 31

7. D. Rapp, P. Englander-Golden, J. Chem. Phys. **43**, 1464 (1965)

8. J. Davis, J.L. Giuliani, Jr., and M. Mulbrandon, Phys. of Plasmas **2**, 1766(1995).

9. J.W.Thornhill, K.G.Whitney, C. Deeney, and P.D. Lapell, Phys Plasmas **1**, 321 (1994).

10. S.I. Braginskii, "Transport Processes in a Plasma", Rev of Plasma Physics Vol. 1, 205, edited. by M.A. Leontovich (Consultants Bureau: New York, 1965).

11. W.D. Schulz, "Two-Dimensional Lagrangian Hydrodynamic Difference Equations", Methods in Computational Physics Vol. 3, 1, edited by B. Alder, S. Fernbach, and M. Rotenberg (Academic Press: New York, 1964).

12. D.D. Hinshelwood NRL Memo Rept 5185 (1983). See National Technical Information Service Document # 135024. Copies may be ordered from the National Technical Information Service, Springfield, Virginia 22161.